

Constant-Volume Deformation Manufacturing for Material-Efficient Shaping

Li Lei^{1†}, Gong Jiale^{2†}, Li Ziyang¹, Wang Hong^{1*}

¹School of Mechanical Engineering and Automation, Northeastern University, Shenyang 110819, China.

Email: lil22@mails.neu.edu.cn (Li Lei)

Email: 2110108@stu.neu.edu.cn (Li Ziyang)

²Future Laboratory, Tsinghua University, Beijing 100084, China.

Email: gongjiale@mail.tsinghua.edu.cn (Gong Jiale)

*Corresponding author. Email: hongwang@mail.neu.edu.cn (Wang Hong)

†These authors contributed equally to this work.

Additive and subtractive manufacturing enable complex geometries but rely on discrete stacking or local removal, limiting continuous and controllable deformation and causing volume loss and shape deviations. We present a volume-preserving digital-mold paradigm that integrates real-time volume-consistency modeling with geometry-informed deformation prediction and an error-compensation strategy to achieve highly predictable shaping of plastic materials. By analyzing deformation patterns and error trends from post-formed point clouds, our method corrects elastic rebound and accumulation errors, maintaining volume consistency and surface continuity. Experiments on five representative geometries demonstrate that the system reproduces target shapes with high fidelity while achieving over 98% material utilization. This approach establishes a digitally driven, reproducible pathway for sustainable, zero-waste shaping of user-defined

designs, bridging digital modeling, real-time sensing, and adaptive forming, and advancing next-generation sustainable and customizable manufacturing.

1

Throughout early technological development, artisans working with malleable materials such as clay (1) and metals mastered shaping techniques (2) based on gradual, volume-preserving deformation. This material-centric logic—linking geometric continuity, material flow, and controllable deformation—formed (3–5) one of the earliest coherent manufacturing principles (6). Although rooted in handcraft, its emphasis on continuity, precision, and volume conservation resonates with modern demands for efficient, low-waste, customizable production (7)s, offering conceptual guidance for today’s digital manufacturing systems (8).

With the rise of Industry 4.0 (9), Germany established a framework centered on inter connectivity, digitization, and intelligent automation, greatly advancing equipment capabilities and system-level integration (10). Yet fundamental limitations remain unresolved. Modern manufacturing is still dominated by subtractive approaches where material waste is inherent (11, 12); mass production struggles to accommodate individualized designs (13); and in complex products, material behavior, process compensation, and digital models remain only loosely connected (14, 15). Even within highly digitalized industrial ecosystems, a key pursuit persists: rebuilding a “volume-preserving, controllable, zero-waste shaping paradigm” (16, 17) analogous to traditional ceramic forming.

Recent trends in green manufacturing, reconfigurable production, and user-centered customization have highlighted opportunities and challenges (18). Additive manufacturing (AM) (19), although alleviating some drawbacks of subtractive processes through geometric freedom and personalization (20), introduces its own limitations: layer-by-layer stacking produces stepping artifacts (21, 22); anisotropy, high energy consumption, long build times, and limited volumetric accuracy hinder scalability (23, 24); and support structures create hidden material waste (25). Crucially, neither subtractive nor additive methods enable continuous deformation control of material during forming (26, 27). As a result, they cannot achieve the volume preservation, stress continuity, or geometric smoothness inherent to traditional hand shaping (28). Despite its geometric versatility,

AM does not fundamentally address key issues of geometric continuity, volume consistency, and controllable deformation in user-defined manufacturing (29).

Looking forward, next-generation manufacturing systems integrating digital molds (30), flexible equipment, reconfigurable robotics (31), and intelligent scheduling aim to surpass the constraints of conventional subtractive and additive methods (32, 33). Such systems seek to map user intent directly into physical production with real-time perception, adaptive forming, and optimal resource utilization. Yet one essential element remains missing: a shaping mechanism capable of maintaining material volume while supporting continuous, controllable deformation. Establishing standardized pipelines through digital modeling, material flow prediction, and deformation compensation (34) can make user-customizable designs truly manufacturable, predictable, and sustainable (35, 36).

To address this gap, we developed an experimental framework for investigating volume-preserving shaping and deformation control. Each trial forms a workpiece with a fixed feed increment, followed by 3D scanning (37) to obtain post-formed point clouds (PCL). Ideal PCL, derived from molding instructions and end-effector trajectories, are compared with target STL PCL to evaluate theoretical accuracy (38, 39). Actual PCL are registered to target PCL to extract deformation modes and error trends. To demonstrate generality, we additionally scanned 3D-printed components, enabling comparative analysis between ideal PCL, printed geometries, and molded workpieces. Material loss is quantified through pre- and post-forming mass and surface-area measurements (40), and the entire shaping process is visually documented. These datasets establish a foundation for volume-preserving and environmentally sustainable manufacturing.

Within the broader context of Industry 4.0 and sustainable production, our study addresses four challenges:

1. Building infrastructure and methodological tools for evaluating the sustainability potential of Industry 4.0 technologies;
2. Managing product configurability and user customization while providing transparent sustainability feedback;
3. enhancing system flexibility through automated reconfiguration and intelligent scheduling;
4. enabling zero-waste green manufacturing through modular, human–robot collaborative systems.

Through experimental validation and methodological analysis, we demonstrate the feasibility of volume-preserving forming and propose a reproducible, digitally driven pathway for user-customizable green manufacturing, offering scientific insight and practical guidance for future sustainable production.

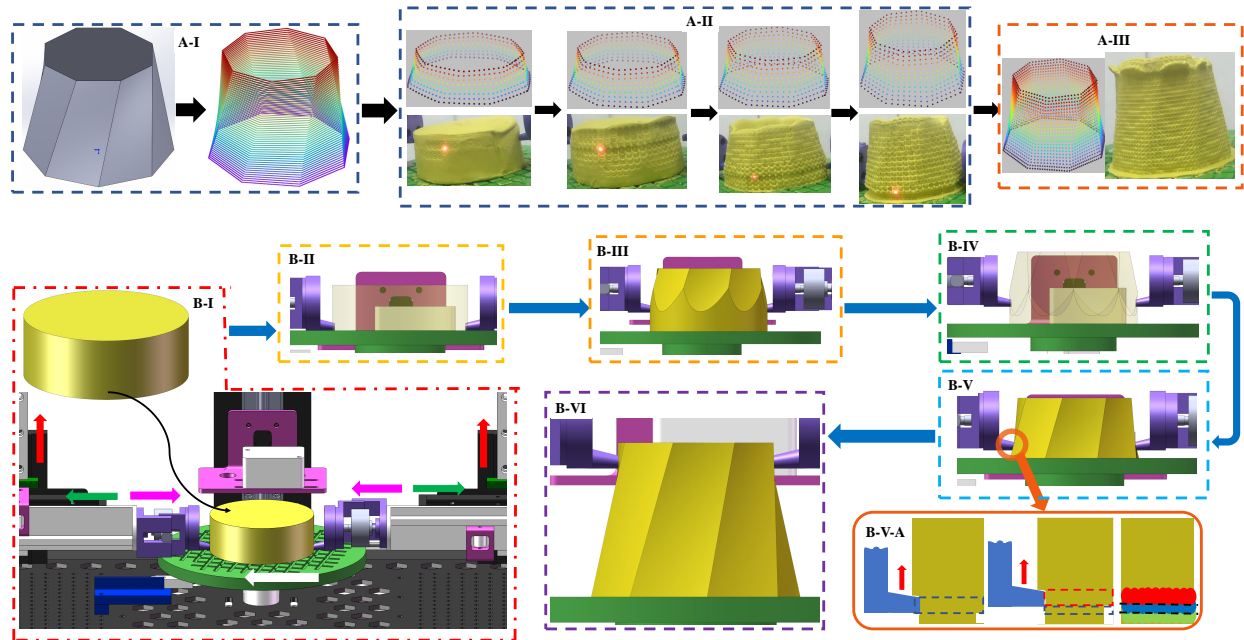


Figure 1: Overview of the intelligent kneading workflow. (A) The complete processing pipeline from extracting PCL from the input STL geometry, generating kneading commands, to the corresponding intermediate workpiece states after each kneading stage. (B) The detailed kneading and forming process of the geometric object, where B-V-A illustrates the effective region applied during each incremental kneading layer.

2 Intelligent Kneading System Design and Workflow

The intelligent kneading system, independently designed and built, integrates hardware Fig. S1, sensing, and control software Fig. S2 (Hardware system and software system design) to reproduce complex three-dimensional geometries with high fidelity Fig. 1. Fig. 1-A-I illustrates the target PCL obtained from the 3D model of each geometry. Fig. 1-A-II shows the process of automatically generating kneading-instruction PCL(point clouds) at different stages, based on the changing size of the workpiece. Fig. 1-A-III presents the PCL from the final kneading step and the resulting kneced geometry. Fig. 1-B shows the physical kneading process performed on the RK3588-based

controlled platform. Fig. 1-B-I illustrates the motion directions of the platform's six degrees of freedom. Fig. 1-B-II to Fig. 1-B-VI depict the deformation of the workpiece from the initial blank to the final kneaded form, where Fig. 1-B-V-A highlights the effect of layer-wise kneading on the workpiece and the corresponding vertical working range (Materials and methods: Designed three types of end-effectors Fig. S9, Fig. S10 and Ideal machining accuracy Fig. S12). The adaptive software pipeline within the system converts three-dimensional models into layer-wise kneading instructions, enabling real-time control and adaptive kneading Fig. S3. This allows the system to reproduce a wide variety of complex shapes without any manual intervention.

Five representative geometries (41) were selected to evaluate the system: a square prism Fig. S4-A, a cylinder Fig. S4-B, Slim Waist Fig. S4-C, a helical truncated octagonal frustum Fig. S4-D, and a concave cylinder Fig. S4-E. For each shape, both the 3D-printed model (left) and the corresponding kneaded geometry (right) are shown, highlighting the system's ability to reproduce simple and complex surfaces. The geometric models are parameterized to extract key features such as cross-sectional radii, torsion angles, and contour continuity, which allow classification into **enveloping** or **non-enveloping** shapes (42) (Tab. S1). This classification informs the choice of kneading strategy: Envelope Shaping First method (43) is applied to enveloping geometries, while Similar Gradient method (44) is applied to non-enveloping geometries.

The kneading process begins with layer-based slicing of the 3D model to extract cross-sectional PCL (45). Each layer is converted to polar coordinates for geometric analysis, which guides the computation of end-effector positions and radial compensation. The system adaptively determines kneading steps and feed depth based on the minimum-radius principle, ensuring continuous shaping and volume consistency. Fig. 1-A shows that the system reproduces complex geometries accurately, with the kneaded results closely matching the 3D-printed reference shapes (from an observational standpoint). This demonstrates that the integrated hardware-software pipeline effectively translates geometric specifications into physical manipulation, highlighting both precision and versatility.

3 Evaluation of Kneading Accuracy and Material Utilization

To evaluate the machining accuracy of the system (38), ideal kneading PCL (Materials and Methods: Ideal machining accuracy) were generated for geometric objects A and B Fig. 2, A1 and B1

simulating theoretical kneading results according to the control commands; geometric objects A and B were processed using the Envelope Shaping First method. For geometric objects C, D, and E Fig. 3, C1, D1, and E1, ideal machining PCL were also generated, and both the Similar Gradient (44) and Envelope Shaping First methods (43) were applied. These ideal PCL were then registered with the target PCL sampled from the STL models(Materials and Methods:Layer-Based Contour Extraction Algorithm from STL Mesh with Convex Hull) using the ICP algorithm.

In Fig. 2-A3, after compensation, the variation trend of RMSE with respect to the threshold becomes closer to the ideal kneading accuracy. When the fitness reaches 1.0, the RMSE value also becomes closer to the ideal kneading accuracy as the threshold increases (Materials and Methods:Geometric A and B kneaded PCL and compensation PCL ICP registration result-Fig. S14). The ICP registration data for geometric object B are shown in Fig. 2-B3. The variation trend after compensation for geometric B is generally consistent with that of geometric A. In particular, for geometric objects A and B, the threshold values at a fitness of 1.0 are very close, both before and after compensation (Materials and Methods:Geometric A and B kneaded PCL and compensation PCL ICP registration result-Fig. S15). From Fig. 2-A3, it can be seen that the RMSE of the theoretical registration I_A converges more slowly with respect to the threshold than that of AM_A , and at a fitness of 1.0, the RMSE value of I_A is greater than that of AM_A . In contrast, in Fig. 2-B3, the RMSE of I_B converges faster with respect to the threshold than AM_B , and at a fitness of 1.0, the RMSE value of I_B is smaller than that of AM_B . The differences between geometric objects A and B arise from the inherent characteristics of the geometries and the specific features of the kneading process. Figures 2-A4 and 2-B4 demonstrate that the differences between the kneaded PCL and the 3D-printed scanned PCL are highly significant.

For geometric objects C, D, and E, two machining methods were applied. The final PCL obtained from both methods were registered with the target PCL, and the RMSE value at the fitness of 1.0 was similarly used as the compensation value for each method. The compensated PCLs were then registered again with the target PCL, respectively. For geometric C, the ICP registration results are shown in Fig. 3-C3. The PCL K_{C1} reaches a fitness of 1.0 at $Threshold = 3.4$, which is smaller than the $Threshold = 3.6$ required for K_{C2} . After compensation(Materials and Methods:Geometry C registered PCL and using two kneading methods model Fig. S18 and Fig. S19), $K_{Scale-C1}$ reaches a fitness of 1.0 at $Threshold = 1.7$, which is smaller than the $Threshold = 2.8$ for $K_{Scale-C2}$

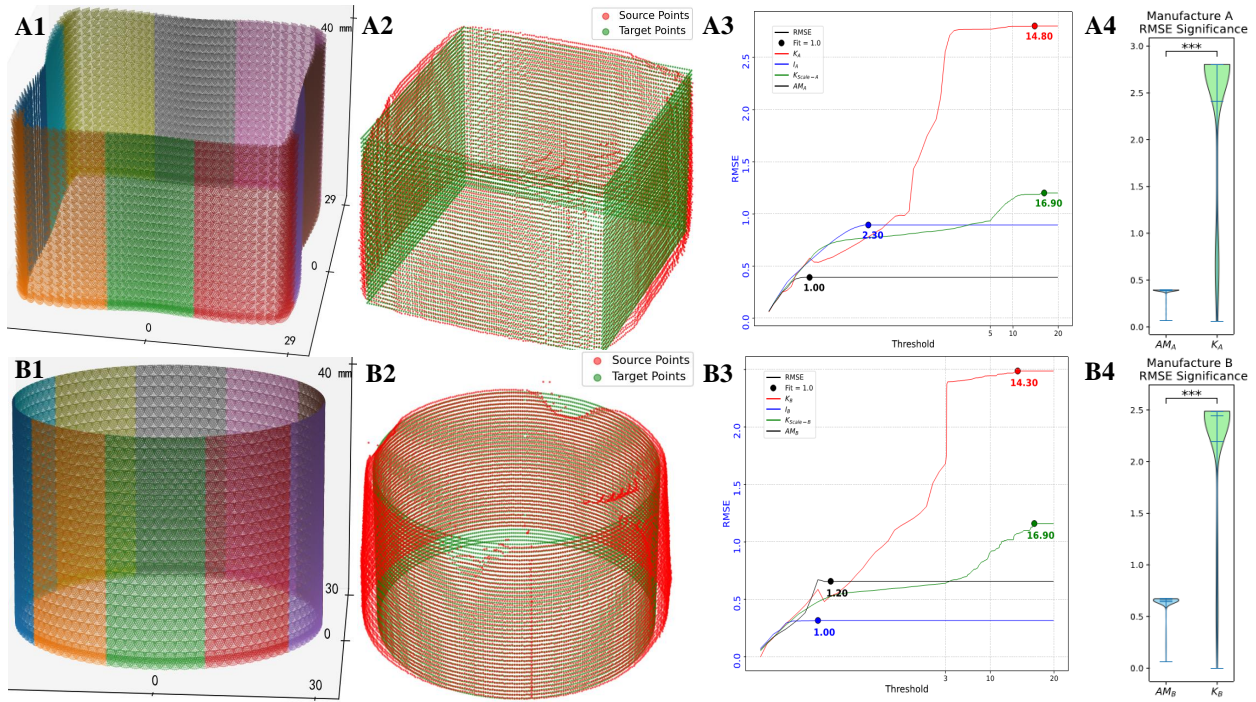


Figure 2: Analysis of kneading accuracy for Geometries A and B. (A1, B1) Ideal machining PCL generated from kneading commands for Geometry A and B. (A2, B2) Actual kneced PCL obtained from the platform. (A3, B3) Line plots showing the registration of ideal PCL, actual kneced PCL, compensated PCL, and 3D-printed PCL against the target PCL. (A4, B4) Statistical significance analysis of differences between actual kneced PCL and 3D-printed PCL with respect to the target PCL. K_A — actual kneced PCL; I_A — ideal kneading PCL; $K_{Scale-A}$ — compensated actual kneced PCL; AM_A — 3D-printed scanned PCL

and is closer to the ideal kneading I_A . As shown in Fig. 3-C3, the compensated PCLs $K_{Scale-C1}$ and $K_{Scale-C2}$ better fit the target PCL. For geometric D, the ICP registration results are shown in Fig. 3-D3. Before compensation, geometric D PCLs K_{D1} and K_{D2} , as well as the compensated $K_{Scale-D1}$ and $K_{Scale-D2}$, all exhibit *Threshold* values at fitness 1.0 that are greater than those of geometric C. After compensation (Materials and Methods: Geometry D registered PCL and using two kneading methods model Fig. S20 and Fig. S21), the RMSE variation curve of $K_{Scale-D2}$ becomes smoother than that of K_{D2} , and the *Threshold* required to reach fitness 1.0 for $K_{Scale-D2}$ becomes larger compared with the pre-compensation K_{D2} . For both geometric C and D, the RMSE values of K_{C1} and K_{D1} are higher than those of K_{C2} and K_{D2} , while after compensation, the RMSE values of $K_{Scale-C1}$ and $K_{Scale-D1}$ become smaller than those of $K_{Scale-C2}$ and $K_{Scale-D2}$. As shown in Fig. 3-D3, the compensated PCLs based on RMSE achieve better alignment with the target PCL compared with the uncompensated ones. For geometric E, the ICP registration results are shown in Fig. 3-E3. Unlike geometric A, B, C, and D, the RMSE variation trends of K_{E1} and K_{E2} remain stable without large jumps, and both reach fitness 1.0 at *Threshold* = 12.8. After compensation (Materials and Methods: Geometry E registered PCL and using two kneading methods model Fig. S22 and Fig. S23), $K_{Scale-E1}$ reaches fitness 1.0 at *Threshold* = 15.7, and $K_{Scale-E2}$ reaches fitness 1.0 at *Threshold* = 15.8, which are very close to each other. Among the five geometric objects A, B, C, D, and E, geometric E is the only one whose *Threshold* values before and after compensation remain the closest when reaching a fitness of 1.0. The RMSE values of $K_{Scale-C1}$, $K_{Scale-D1}$, and $K_{Scale-E1}$ at a fitness of 1.0 are smaller than those of AM_C , AM_D , and AM_E , respectively. In contrast, the RMSE values of $K_{Scale-C2}$, $K_{Scale-D2}$, and $K_{Scale-E2}$ are all greater than those of the 3D-printed scanned point clouds. Moreover, as shown in Fig. 3-C4, D4, and E4, the differences between the 3D-printed results and the two machining methods are extremely significant, and the differences between the two machining methods themselves are also extremely significant.

Tab. S3 summarizes the convergence thresholds and final RMSE values for registering the actual kneaded PCL, ideal PCL, and 3D-printed scanned PCL of the five geometries. The analysis shows that the compensated actual kneaded PCL exhibit significantly reduced errors relative to the target PCL, whereas the 3D-printed PCL achieve relatively high fitting accuracy. Furthermore, comparison of the two kneading methods indicates that the Similar Gradient method achieves

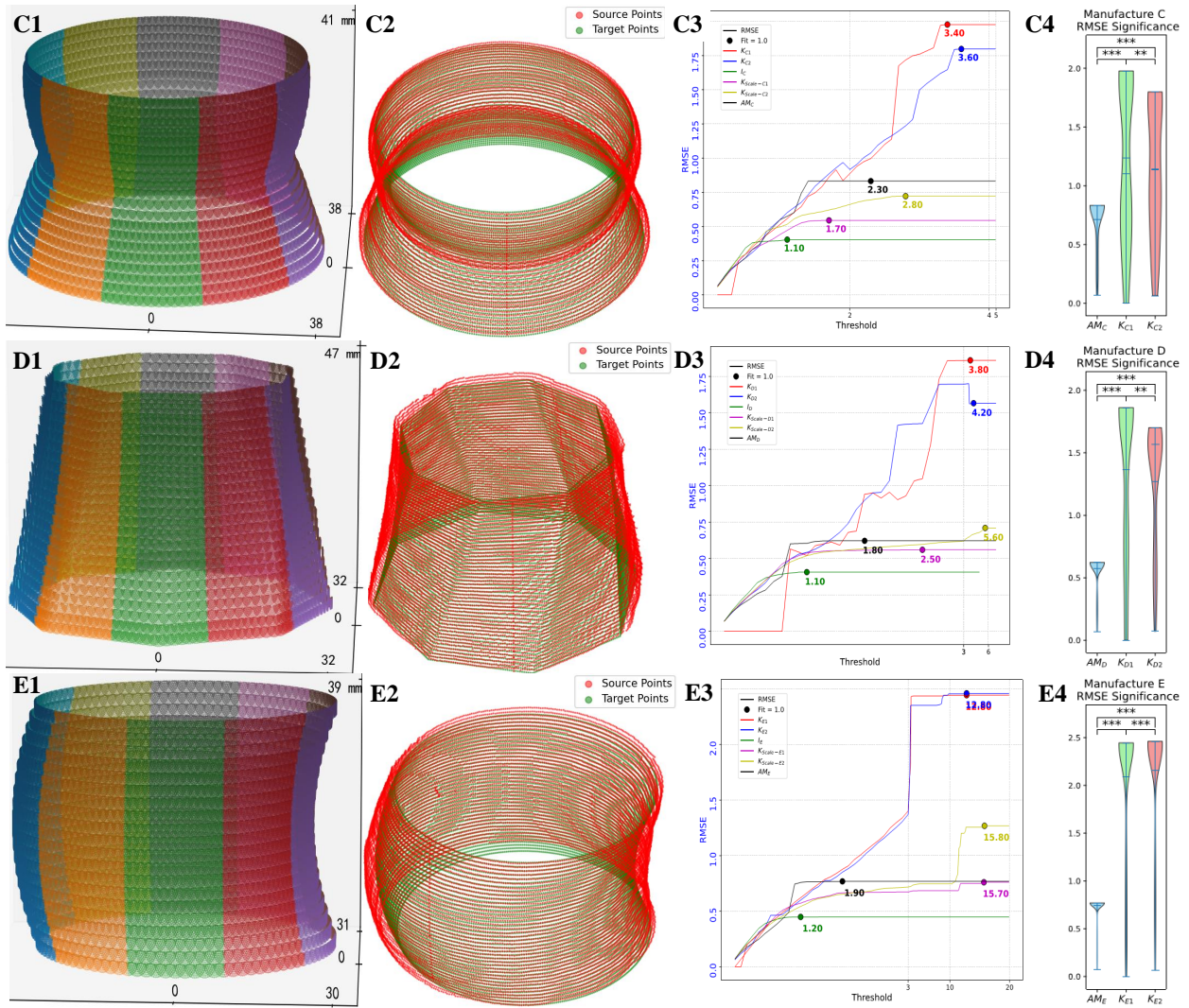


Figure 3: Analysis of kneading accuracy for Geometries C, D, and E. (C1, D1, E1) Ideal machining PCL generated from kneading commands for Geometries C, D, and E. **(C2, D2, E2)** Actual kneaded PCL obtained from the platform using two different kneading methods. **(C3, D3, E3)** Line plots showing the registration of ideal PCL, actual kneaded PCL from both methods, compensated PCL corresponding to each method, and 3D-printed PCL against the target PCL. **(C4, D4, E4)** Statistical significance analysis of differences between actual kneaded PCL from both methods and 3D-printed PCL with respect to the target PCL. K_{C1} — **actual kneaded PCL using Similar Gradient method** K_{C2} — **actual kneaded PCL using Envelope Shaping First method** I_C — **ideal kneading PCL** $K_{Scale-C1}$ — **compensated actual kneaded PCL using Similar Gradient method** $K_{Scale-C2}$ — **compensated actual kneaded PCL using Envelope Shaping First method** AM_C — **3D-printed scanned PCL**

faster convergence of RMSE, and after compensation, both RMSE values for the Similar Gradient method are smaller than those of the Envelope Shaping First method, highlighting the importance of selecting a kneading strategy matched to the geometric features, .

We measured the material mass before and after kneading for all geometries Fig. 4-I. The results show that the average material utilization exceeds 98%, with the maximum material loss remaining below 5 g. For Geometries C, D, and E, the mass loss under the two kneading methods is nearly identical, indicating that the two strategies exhibit no significant difference in terms of material efficiency.

Fig. 4-II summarizes the required processing cycles and total kneading time for each geometry. The initial billets for Geometries A, C, and E were cylindrical disks with an 80 mm diameter (shown in Fig. 4, Fig. 4-III- $K_A - 1$, Fig. 4-III- $K_{C1} - 1$, and Fig. 4-III- $K_{E1} - 1$, respectively). Geometry B used a cube with an 84.5 mm diagonal as the billet, while Geometry D used a 75 mm diameter disk. The number of required processing cycles is determined primarily by the difference between the maximum initial billet dimension and the minimum dimension of the target geometry. Geometry A exhibited the largest difference (16.5 mm), resulting in the highest number of cycles and the longest kneading time. For Geometry C, the kneading time for both methods was similar. Geometry D required approximately 1 hour more when using the Similar Gradient method than when using the Envelope Shaping First method, whereas Geometry E required about 2 hours more under the Envelope Shaping First method than under the Similar Gradient method. These findings indicate that, under the same billet size and processing-cycle count, the geometric characteristics of the object themselves dictate the overall processing time.

Fig. 4-IV-A through Fig. 4-IV-E illustrate the evolution of the lateral surface area (i.e., the curved surface perpendicular to the XOY plane) as kneading progresses. The overall surface-area evolution patterns are similar across geometries. Notably, Geometry B achieves a final kneaded surface area closest to its ideal model. This is because its billet—a cube with a 60 mm edge and an 84 mm diagonal—closely approximates the circumscribed quadrilateral of the target cylinder (diameter 60 mm, height 40 mm). Moreover, the billet height is close to the target height, resulting in minimal deformation along the Z-axis and consequently a final surface area very close to the ideal geometry.

In contrast, the final surface areas of Geometries A, C, D, and E exceed those of their ideal

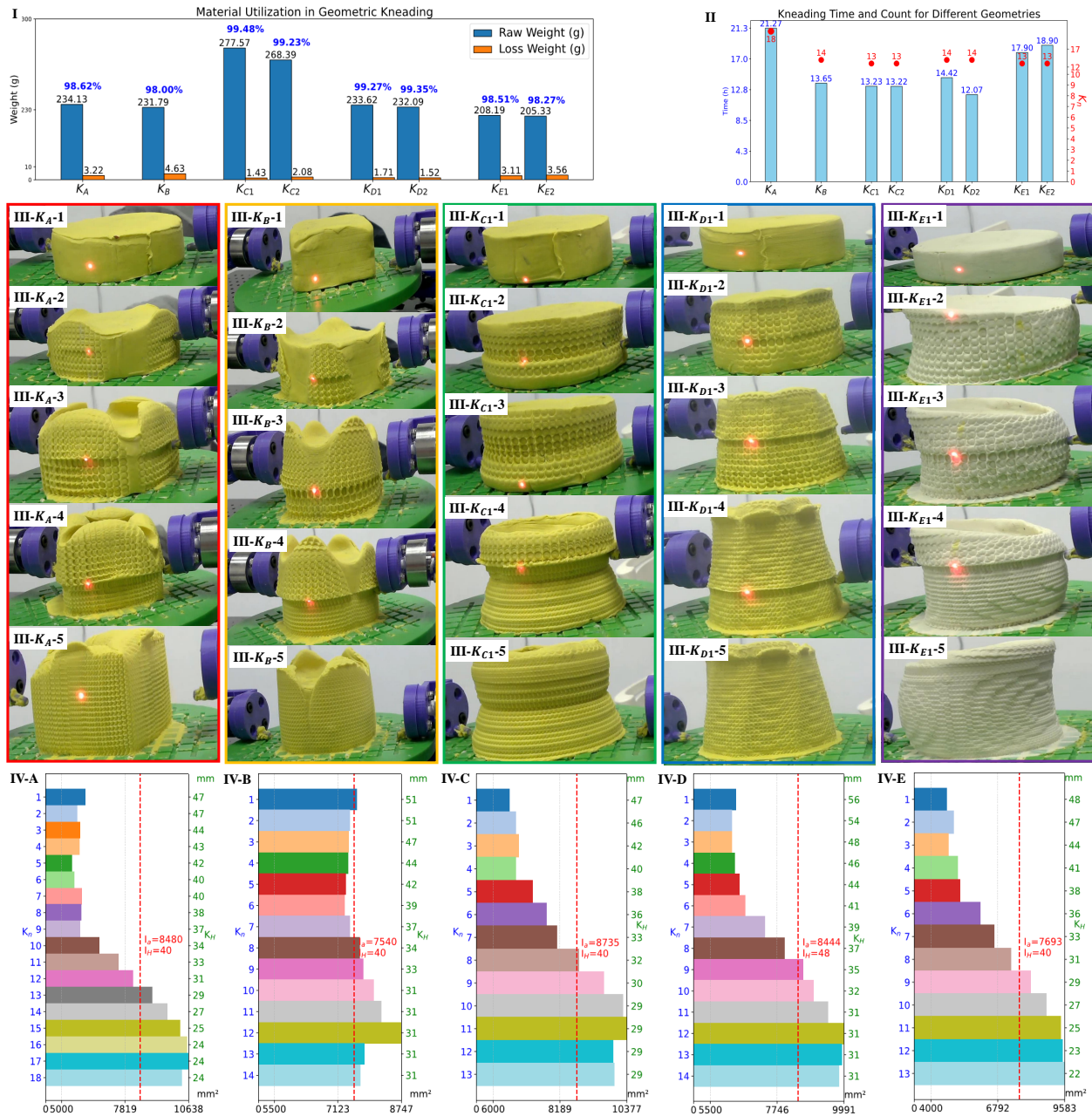


Figure 4: Analysis of kneading process and material utilization. (I) Material quality and utilization for Geometries A, B, C, D, and E, including material lost after kneading. **(II)** Kneading time and number of processing cycles for each geometry. **(III)** Visualization of the kneading formation process for each geometry. **(IV-A, IV-B, IV-C, IV-D, IV-E)** Surface area evolution during the kneading process for Geometries A, B, C, D, and E; red lines indicate the surface area of the target geometry. **(K.C1)** Demonstrates the geometry kneaded using the Similar Gradient method.

models. This is due to two effects: (1) elastic rebound of the material increases the final cross-sectional dimensions; and (2) axial upward material accumulation during kneading produces a hollowed upper region, yielding a final height greater than the target geometry. Together, these factors lead to final kneaded surface areas consistently larger than their ideal counterparts.

4 Conclusions

We developed a volume-preserving digital-mold shaping paradigm that enables continuous and controllable deformation of plastic materials, overcoming inherent limitations of conventional additive and subtractive manufacturing. By integrating real-time volume-consistency modeling, geometry–stress coupled deformation prediction, and a unified compensation strategy, the system accurately reproduces complex user-defined geometries while mitigating error accumulation and elastic rebound. Experimental validation across five representative shapes demonstrates high fidelity, with compensated kneading results closely matching target geometries and achieving material utilization above 98%. The selection of geometry-adaptive kneading strategies, including Envelope Shaping First and Similar Gradient methods, further optimizes accuracy and efficiency, highlighting the importance of matching process parameters to geometric features.

These results establish a reproducible, digitally driven pathway for sustainable, zero-waste shaping of user-customized designs. By bridging digital models, real-time sensing, and adaptive forming, this paradigm provides a methodological foundation for green manufacturing, reconfigurable production, and user-driven customization, advancing the capabilities of next-generation sustainable manufacturing systems.

References and Notes

1. R. Montesana, F. Iacono, R. Guglielmino, Crafting resilience: persistence and adaptation of the ceramic manufacture at Roca Vecchia from the Middle to the Final Bronze Age phases. *Archaeological and Anthropological Sciences* **16** (6), 89 (2024).
2. D. M. Stefanescu, A succinct history of metalcasting knowledge. *International Journal of Metalcasting* **17** (4), 2373–2388 (2023).
3. M.-G. Lee, Y. P. Korkolis, *Advances in plastic forming of metals* (2018).
4. G. Faraji, H. Torabzadeh, An overview on the continuous severe plastic deformation methods. *Materials transactions* **60** (7), 1316–1330 (2019).
5. L. Donati, B. Reggiani, R. Pelaccia, M. Negozio, S. Di Donato, Advancements in extrusion and drawing: a review of the contributes by the ESAFORM community. *International Journal of Material Forming* **15** (3), 41 (2022).
6. X. Zhang, Y. Wang, Y. Liang, Q. Wang, Material characterization of forged bronzes from ancient China (c. 11th-2nd century BCE) reveals development of the non-mainstream metalworking technique in Chinese bronze production. *Journal of Archaeological Science* **172**, 106108 (2024).
7. P. Oakley, Materials sustainability across the crafts and applied arts: A review and reflections. *Sustainable Innovation 2023* (2024).
8. J. A. Stein, The production of toolboxes and hand tools in industrial craft apprenticeship. *The Journal of Modern Craft* **12** (3), 233–254 (2019).
9. H. Kagermann, W. Wahlster, Ten years of Industrie 4.0. *Sci* **4** (3), 26 (2022).
10. M. Hankel, B. Rexroth, The reference architectural model industrie 4.0 (rami 4.0). *Zvei* **2** (2), 4–9 (2015).
11. L. Proud, D. Whitehead, T. Slatter, P. Crawforth, D. Curtis, Subtractive Manufacturing of Hazardous Materials: A Review. *Safety* **11** (4), 112 (2025).

12. G. Ingarao, P. C. Priarone, F. Gagliardi, R. Di Lorenzo, L. Settineri, Subtractive versus mass conserving metal shaping technologies: an environmental impact comparison. *Journal of Cleaner Production* **87**, 862–873 (2015).
13. B. Freitas, *et al.*, A review of hybrid manufacturing: integrating subtractive and additive manufacturing. *Materials* **18** (18), 4249 (2025).
14. K. Nagayama, J. Yan, Deterministic error compensation for slow tool servo-driven diamond turning of freeform surface with nanometric form accuracy. *Journal of Manufacturing Processes* **64**, 45–57 (2021).
15. B. Iñigo, N. Colinas-Armijo, L. N. López de Lacalle, G. Aguirre, Digital Twin for Volumetric Thermal Error Compensation of Large Machine Tools. *Sensors* **24** (19), 6196 (2024).
16. J. Lario, J. Mateos, F. Psarommatis, Á. Ortiz, Towards Zero Defect and Zero Waste Manufacturing by Implementing Non-Destructive Inspection Technologies. *Journal of Manufacturing and Materials Processing* **9** (2), 29 (2025).
17. H. Pu, *et al.*, A Sustainable Manufacturing Paradigm to Address Grand Challenges in Sustainability and Climate Change. *ACS Sustainable Resource Management* **1** (11), 2334–2337 (2024).
18. M. Todescato, *et al.*, Sustainable manufacturing through application of reconfigurable and intelligent systems in production processes: a system perspective. *Scientific Reports* **13** (1), 22374 (2023).
19. L. Zhou, *et al.*, Additive manufacturing: a comprehensive review. *Sensors* **24** (9), 2668 (2024).
20. K. Yu, M. L. Dunn, H. Jerry Qi, K. Maute, Recent advances in design optimization and additive manufacturing of composites: from enhanced mechanical properties to innovative functionalities. *npj Advanced Manufacturing* **2** (1), 1–13 (2025).
21. A. P. Golhin, R. Tonello, J. R. Frisvad, S. Grammatikos, A. Strandlie, Surface roughness of as-printed polymers: a comprehensive review. *The International Journal of Advanced Manufacturing Technology* **127** (3), 987–1043 (2023).

22. A. Mathew, *et al.*, Vapour polishing of fused deposition modelling (FDM) parts: a critical review of different techniques, and subsequent surface finish and mechanical properties of the post-processed 3D-printed parts. *Progress in Additive Manufacturing* **8** (6), 1161–1178 (2023).
23. Z. Kong, *et al.*, Mechanical properties of SLM 316L stainless steel plate before and after exposure to elevated temperature. *Construction and Building Materials* **444**, 137786 (2024).
24. R. D. Kundu, X. S. Zhang, Additive manufacturing of stiff and strong structures by leveraging printing-induced strength anisotropy in topology optimization. *Additive Manufacturing* **75**, 103730 (2023).
25. J. Jiang, X. Xu, J. Stringer, Support structures for additive manufacturing: a review. *Journal of Manufacturing and Materials Processing* **2** (4), 64 (2018).
26. W. Wang, F. van Keulen, J. Wu, Fabrication sequence optimization for minimizing distortion in multi-axis additive manufacturing. *Computer Methods in Applied Mechanics and Engineering* **406**, 115899 (2023).
27. Y. Zheng, P. Hu, M. Wang, X. Huang, Prediction model for the evolution of residual stresses and machining deformation of uneven milling plate blanks. *Materials* **16** (18), 6113 (2023).
28. U. Yoo, A. Hung, J. Francis, J. Oh, J. Ichnowski, Ropotter: Toward robotic pottery and deformable object manipulation with structural priors, in *2024 IEEE-RAS 23rd International Conference on Humanoid Robots (Humanoids)* (IEEE) (2024), pp. 843–850.
29. Y. Yang, *et al.*, Elasto-plastic residual stress analysis of selective laser sintered porous materials based on 3D-multilayer thermo-structural phase-field simulations. *Npj Computational Materials* **10** (1), 117 (2024).
30. S. Nasiri, M. R. Khosravani, T. Reinicke, J. Ovtcharova, Digital twin modeling for smart injection molding. *Journal of Manufacturing and Materials Processing* **8** (3), 102 (2024).
31. S. Inoue, *et al.*, High-precision mobile robotic manipulator for reconfigurable manufacturing systems. *International Journal of Automation Technology* **15** (5), 651–660 (2021).

32. F. Mo, H. U. Rehman, J. C. Chaplin, D. Sanderson, S. Ratchev, Digital twin-based self-learning decision-making framework for industrial robots in manufacturing. *The International Journal of Advanced Manufacturing Technology* pp. 1–20 (2025).
33. Y. Xia, M. Shenoy, N. Jazdi, M. Weyrich, Towards autonomous system: flexible modular production system enhanced with large language model agents, in *2023 IEEE 28th International Conference on Emerging Technologies and Factory Automation (ETFA)* (IEEE) (2023), pp. 1–8.
34. L. Chen, X. Yao, K. Liu, C. Tan, S. K. Moon, Multisensor fusion-based digital twin in additive manufacturing for in-situ quality monitoring and defect correction. *Proceedings of the design society* **3**, 2755–2764 (2023).
35. C. Martínez-Olvera, Towards the development of a digital twin for a sustainable mass customization 4.0 environment: a literature review of relevant concepts. *Automation* **3** (1), 197–222 (2022).
36. D. Braun, *et al.*, A graph-based knowledge representation and pattern mining supporting the Digital Twin creation of existing manufacturing systems, in *2022 IEEE 27th International Conference on Emerging Technologies and Factory Automation (ETFA)* (IEEE) (2022), pp. 1–4.
37. M. Javaid, *et al.*, Studies on the Metrological need and capabilities of 3D scanning technologies. *Journal of Industrial Integration and Management* **8** (03), 321–339 (2023).
38. L. Li, Z. Li, H. Wang, J. Gong, Design and Error Analysis of a Dual-Degree-of-Freedom 3D Scanner Based on Laser Range Sensors. *Engineering Research Express* (2025).
39. Y. Sun, Z. Shi, B. Yu, M. Li, Line Laser 3D Measurement Method and Experiments of Gears, in *Photonics* (MDPI) (2025), p. 782.
40. Area of the surface, materials and Methods:Area of the surface.
41. Design of the 3D Model for Kneading Geometry, materials and Methods:Design of the 3D Model for Kneading Geometry.

42. Determination of Whether a Geometry is an Enveloping Type, materials and Methods:Determination of Whether a Geometry is an Enveloping Type.
43. Envelope shaping first, materials and Methods:Envelope shaping first.
44. Similar gradient method, materials and Methods:Similar gradient method.
45. Geometric Point Cloud Processing for Kneading Generation, materials and Methods:Geometric Point Cloud Processing for Kneading Generation.

Acknowledgments

Thank the junior and senior members of Group 537, School of Mechanical Engineering and Automation, Northeastern University, for their assistance, and thank the faculty and students of the Future Laboratory, Tsinghua University, for their support.

Funding:

Author contributions: L.L. designed the mechanical structure, developed the hardware–software system, and performed data acquisition. G.J.L. conceived the core ideas and theoretical framework, and provided funding and equipment support. L.Z.Y. conducted data processing, analysis, and manuscript formatting. H.W. organized the manuscript structure and revised the content.

Competing interests: There are no competing interests to declare.

Data and materials availability: The datasets, videos, and software used in this study are available from the corresponding author upon reasonable request. In the final published version, all digital materials will be deposited in a public repository (e.g., Zenodo) with a DOI to ensure reproducibility.

Supplementary materials

Materials and Methods

Materials and methods: Designed three types of end-effectors

Materials and Methods: Ideal machining accuracy

Materials and Methods: Layer-Based Contour Extraction Algorithm from STL Mesh with Convex Hull

Materials and Methods: Geometric A and B kneaded PCL and compensation PCL ICP registration result

Materials and Methods: Geometry C registered PCL and using two kneading methods model

Materials and Methods: Geometry D registered PCL and using two kneading methods model

Materials and Methods: Geometry E registered PCL and using two kneading methods model

Figures S1 to S23

Tables S1 to S3

References (7-45)

Supplementary Materials for Constant-Volume Deformation Manufacturing for Material-Efficient Shaping

Li Lei[†], Gong Jiale[†], Li Ziyang, Wang Hong*

*Corresponding author. Email: hongwang@mail.neu.edu.cn

[†]These authors contributed equally to this work.

This PDF file includes:

Materials and Methods

Materials and methods: Designed three types of end-effectors

Materials and Methods: Ideal machining accuracy

Materials and Methods: Layer-Based Contour Extraction Algorithm from STL Mesh with Convex Hull

Materials and Methods: Geometric A and B kneaded PCL and compensation PCL ICP registration result

Materials and Methods: Geometry C registered PCL and using two kneading methods model

Materials and Methods: Geometry D registered PCL and using two kneading methods model

Materials and Methods: Geometry E registered PCL and using two kneading methods model

Figures S1 to S23

Tables S1 to S3

Materials and Methods

4.0.1 Hardware system and software system design

Independently designed and built the mechanical structure, sensor system, and control system of the intelligent kneading device; developed the lower computer kneading controller software system, the upper computer software system for PCL sampling, processing, and comparative analysis, as well as the automatic kneading instruction generation software system.

Using RK3588 (ROCKCHIP, Fuzhou, Fujian, China) as the lower computer controller, equipped with a 128 GB solid-state drive (Yangtze Memory Technologies, Wuhan, Hubei, China) and 8 GB of RAM (Samsung Electronics, Suwon, Gyeonggi-do, South Korea), and runs an Ubuntu 20.04 development environment. RK3588 communicates with the laser distance sensor (BOJKE, Shenzhen, Guangdong, China), measurement range: $\pm 80\text{mm}$, measurement accuracy: 0.2mm , maximum data acquisition frequency: 100Hz ; via the RS485 (MAXIM, California, United States) protocol and with two Arduino Uno boards (Arduino AG, Ivrea, Italy) via serial and RS232 (EIA, Washington D.C., United States) connections, respectively. The two Arduinos run an improved version of the Arduino CNC firmware, controlling five 28-stepper motors (SUHENG, YanCheng, JiangSu, China), step angle 1.8° , rated current 0.8A, holding torque $0.08\text{N} \cdot \text{m}$; one 57-stepper motor (YINGPENG, Shenzhen, Guangdong, China), step angle 1.8° , rated current 4.5A, holding torque $0.5\text{N} \cdot \text{m}$, based on feedback from six inductive proximity switches (SUHENG, YanCheng, JiangSu, China), output mode of the inductive proximity switch is 1/0. Four fans (YIHE, PuNing, Guangdong, China) are used to cool the two horizontally moving 28-step stepper motors. The entire system is powered by a 220VAC to 24V20A DC switching power (HONGMING, Zhongshan, Guangdong, China) supply. Complete system as Fig .S1.

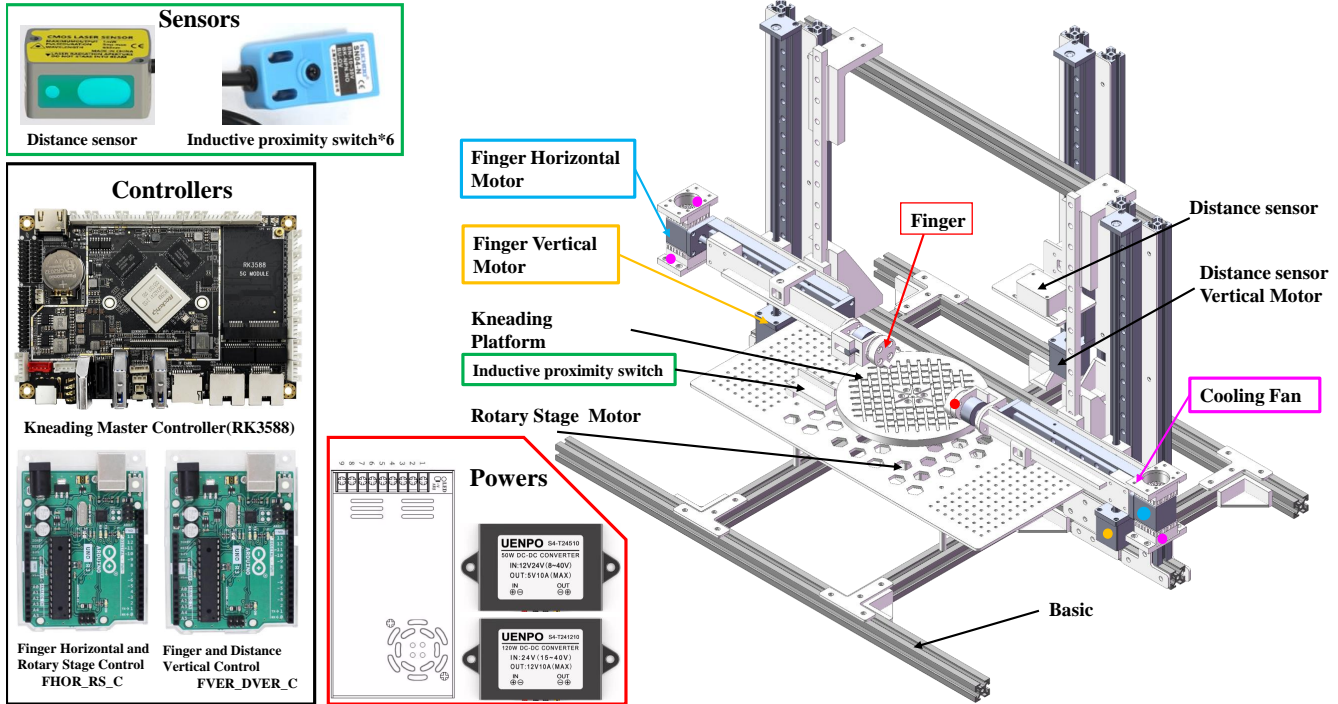


Figure S1: Hardware structure diagram

Main relationship and physical components of the kneading sensor and control system in Fig. S2. The RK3588 controls the *FHOR_RS_C* and *FVER_DVER_C* based on the “Kneading Instruction Set” received from the upper computer, using G-code commands. The *FHOR_RS_C* is responsible for controlling the horizontal movement of the left and right fingers as well as the rotation of the rotary stage, while the *FVER_DVER_C* controls the vertical motion of the two fingers and the distance sensor.

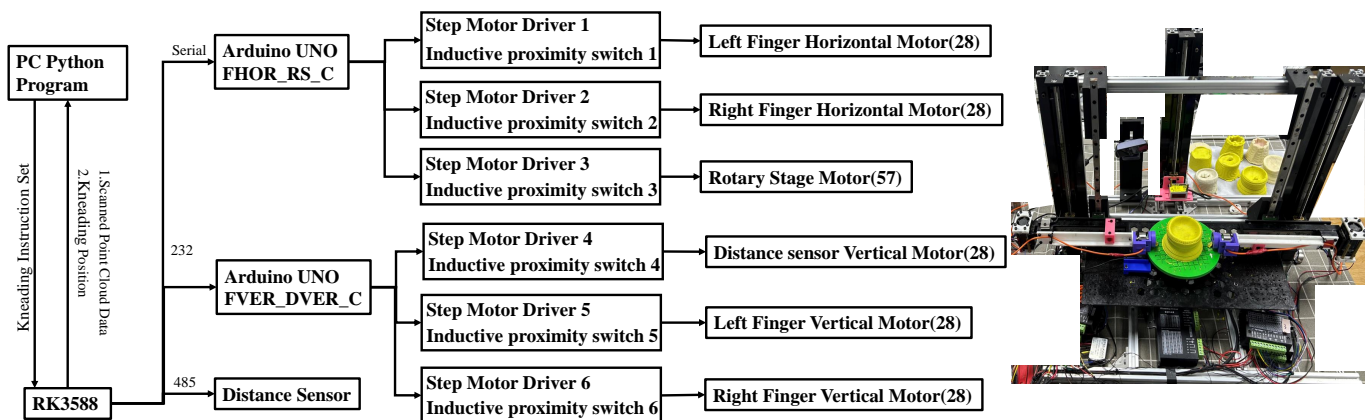


Figure S2: Control and sensor system relationship diagram

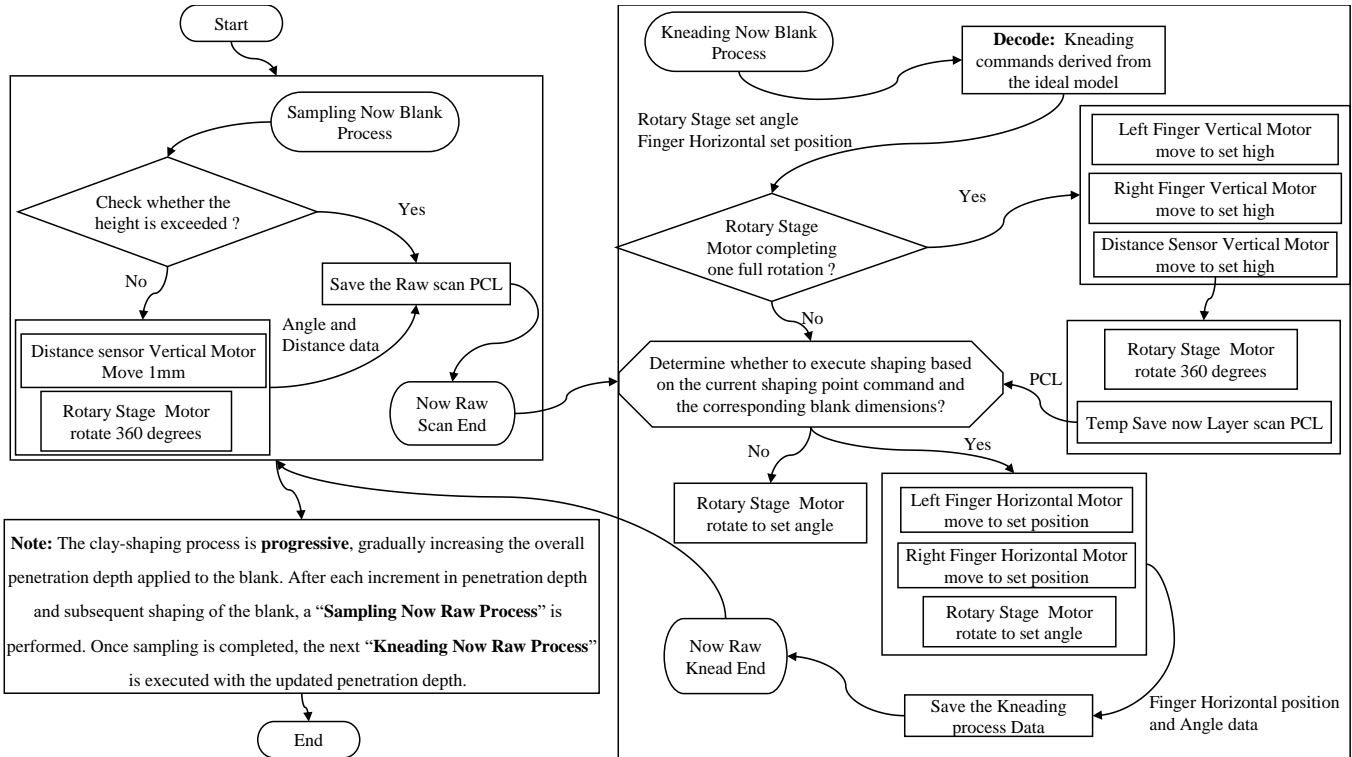


Figure S3: Control flowchart

During the kneading process, the *FHOR_RS_C* uploads the horizontal position data of the fingers to the RK3588, which stores the data. After completing the kneading operation for the current layer, the *FVER_DVER_C* moves the fingers and the sensor upward to perform kneading on the next layer. After each complete kneading operation corresponding to the preset feeding depth, the distance sensor performs a full scan of the kneaded object. Working together with the *FHOR_RS_C*, the system records the rotary stage motor angle and distance sensor data, forming a PCL dataset. The complete control flow is illustrated in Fig. S3.

4.0.2 Design of the 3D Model for Kneading Geometry

Five geometric models were designed, including a square prism with a base side length of 53 mm and a height of 40 mm, a cylinder with a diameter of 60 mm and a height of 40 mm, as well as three geometrically complex shapes: the Slim Waist, Helical Truncated Octagonal Frustum, and Concave Cylinder. The geometric parameters of these three complex geometries are provided in Sections 4.0.2, 4.0.2 and 4.0.2. Fig. S4 show the geometries modeled in SolidWorks and the

corresponding physical objects fabricated using a Bambu Lab 3D printer.

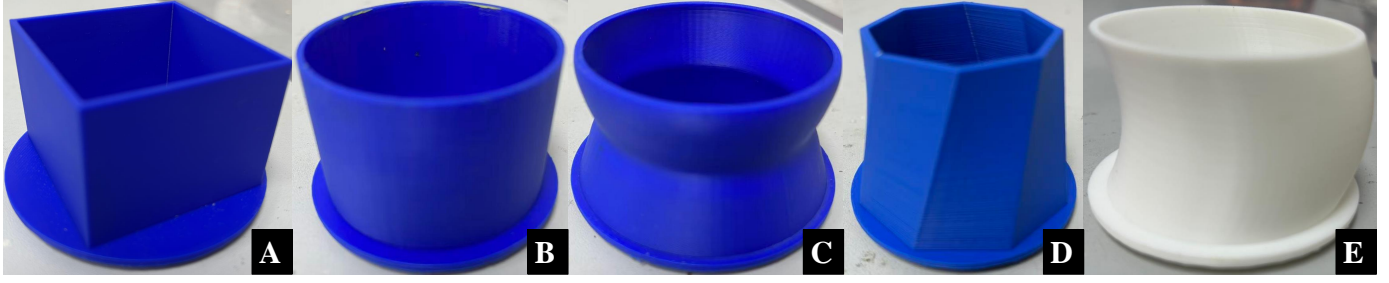


Figure S4: The 3D-printed geometry

Slim waist math equation Slim waist the curve is generated using the spline curve feature in SolidWorks software, which is a B-spline curve. A two-dimensional cubic B-spline is used. The formula is as follows: let the control points be $P_i = (x_i, y_i)$, $i = 0, \dots, 8$, and the degree be $p = 3$, $P_i = (x_i, y_i)$ and 3D model in Fig .S5. Let $C(t)$ denote the point on the spline curve corresponding to the parameter t , where $N_{i,3}(t)$ is the cubic B-spline basis function. The parametric form of the B-spline is Equ.S1, Here, $N_{i,3}(t)$ denotes the cubic B-spline basis function, defined recursively by the Cox–de Boor formula. $N_{i,0}(t)$ is the zero-degree basis function is Equ.S2, and $N_{i,p}(t)$ represents the B-spline basis function of degree p associated with the i -th control point P_i is Equ.S3. In these expressions, t is the curve parameter, i is the control point index, p is the degree of the basis function, and u_i denotes the i -th knot.

$$C(t) = \sum_{i=0}^8 N_{i,3}(t) P_i, \quad t \in [0, 1] \quad (S1)$$

$$N_{i,0}(t) = \begin{cases} 1, & \text{if } u_i \leq t < u_{i+1} \\ 0, & \text{otherwise} \end{cases} \quad (S2)$$

$$N_{i,p}(t) = \frac{t - u_i}{u_{i+p} - u_i} N_{i,p-1}(t) + \frac{u_{i+p+1} - t}{u_{i+p+1} - u_{i+1}} N_{i+1,p-1}(t) \quad (S3)$$

The curve generated by the B-spline is revolved around the Zaxis to create the slim-waist surface, where the radius of the surface at each point corresponds to the points on the B-spline curve is Equ.S4, the R_i is each control point. Parametric equation of the slim-waist surface is Equ.S5.

$$r(z) = \sum_{i=0}^n N_{i,3}(t(z)) R_i, t(z) = \frac{z - z_{\min}}{z_{\max} - z_{\min}} \quad (\text{S4})$$

$$X(\theta, z) = (x, y, z) = (r(z) \cos \theta, r(z) \sin \theta, z), \quad \theta \in [0, 2\pi), z \in [0, h] \quad (\text{S5})$$

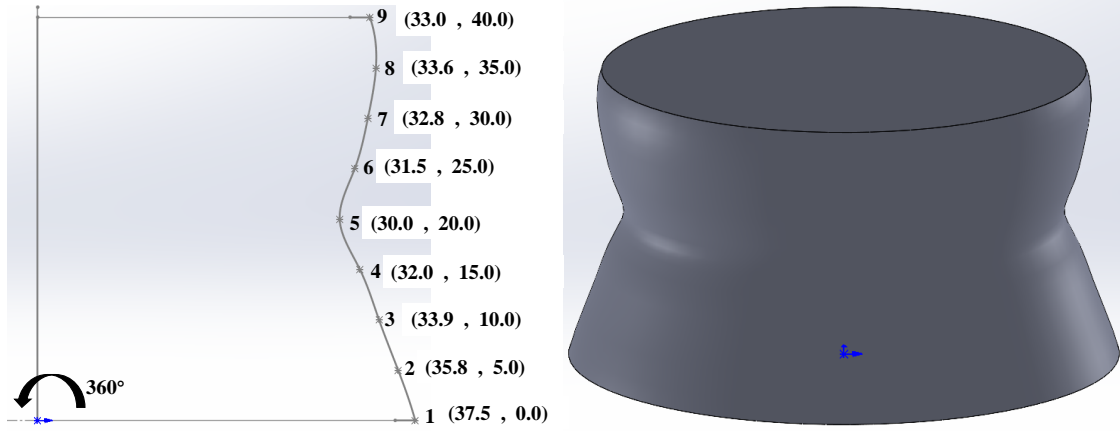


Figure S5: Constraint points and 3D model of the slim waist curve

Helical truncated octagonal frustum math equation Let the total height be h , the number of layers be N , the inradius of the upper inscribed octagon be r_1 , the inradius of the lower inscribed octagon be r_2 , and the total twist angle be Θ , in Fig .S6 (i.e., the rotation of the lower base relative to the upper base) . For the k -th layer, the parameters are defined as follows: the parameter t is a normalized variable (typically mapped along the height direction, either $0 \sim 1$ or $0 \sim N$ layers); $r(t)$ is the radius function that determines the cross-sectional size of the layer and can represent either a linear frustum or a curved variation; $z(t)$ is the height function that gives the coordinate along the Z -axis; $\theta(t)$ is the accumulated twist angle along the height that governs the helical or torsional behavior, is Equ.S6. And ϕ_i is the initial angular position of the i -th vertex before twisting, the k layers i nodes is Equ.S7

$$\begin{cases} t = \frac{N}{k}, \\ r(t) = r_1 + (r_2 - r_1)t, \\ \theta(t) = \Theta t, z(t) = ht \end{cases} \quad (\text{S6})$$

$$\begin{cases} \phi_i = \frac{8\pi}{2}i, \\ P_{k,i} = (r(t) \cos(\phi_i + \theta(t)), r(t) \sin(\phi_i + \theta(t)), z(t)) \end{cases} \quad (S7)$$

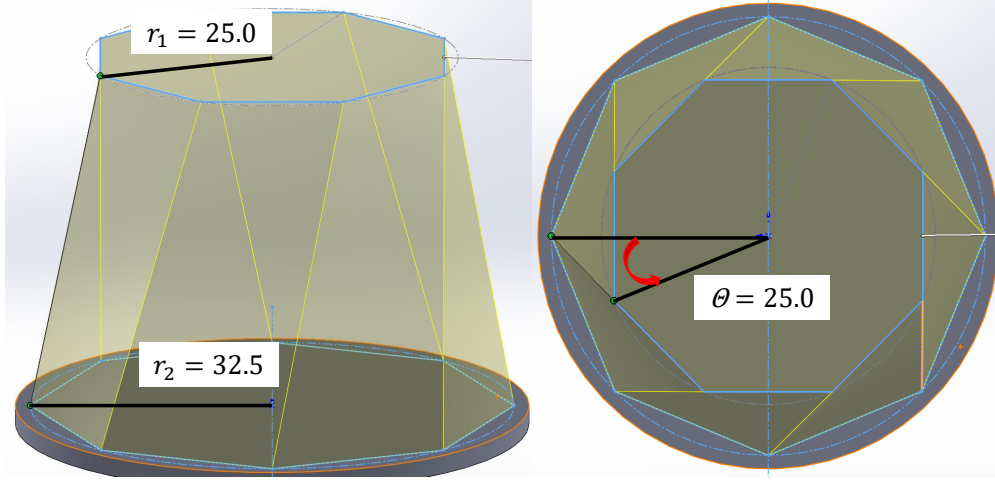


Figure S6: Helical truncated octagonal frustum params and model

Concave cylinder math equation Concave cylinder use SolidWorks drawing, the surface is generated by lofting through three points: $P_0 = (0, r, 0)$, $P_m = (0, y_0 + r, \frac{h}{2})$, $P_h = (0, r, h)$, in Fig .S7. Let the center of the circle be denoted by C , and its trajectory by $C(z)$ is Equ.S8, $d(z)$ is Equ.S9. The parametric formulation of a concave cylinder is Equ.S10

$$C(z) = (0, d(z), z), z \in [0, h] \quad (S8)$$

$$d(z) = 4y \cdot \frac{z}{h} \left(1 - \frac{z}{h}\right) \quad (S9)$$

$$\mathbf{X}(\theta, z) = (x(\theta, z), y(\theta, z), z) = (r \cos \theta, d(z) + r \sin \theta, z) \quad (S10)$$

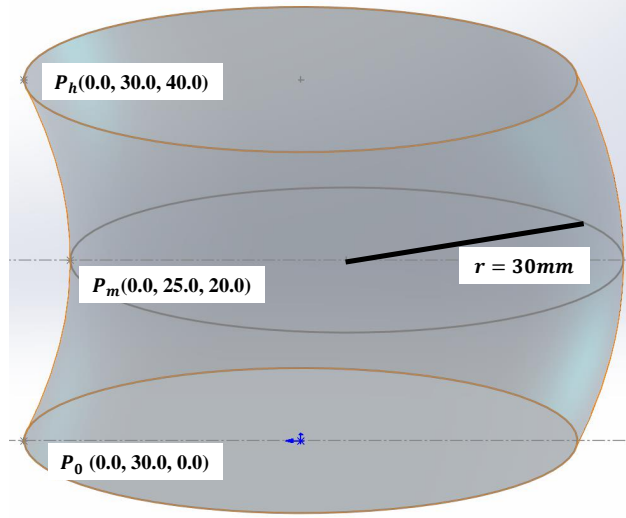


Figure S7: Concave cylinder params and model

4.0.3 Geometric Point Cloud Processing for Kneading Generation

Layer-Based Contour Extraction Algorithm from STL Mesh with Convex Hull The STL mesh model consists of a large number of triangular facets that describe the surface geometry of a 3D object. To extract cross-sectional contours for subsequent analysis or manufacturing simulation, a layer-based contour extraction algorithm is applied. The algorithm slices the STL model along the vertical Z direction with a fixed layer thickness of $\Delta h = 0.1$ mm. For each slicing plane at height $z = h_i$, the intersection between the plane and the mesh is computed. For a triangular facet with vertices $P_1(x_1, y_1, z_1)$, $P_2(x_2, y_2, z_2)$, $P_3(x_3, y_3, z_3)$, the plane intersects the triangle if satisfies Equ.S11.

$$\begin{cases} (z_1 - h_i)(z_2 - h_i) < 0 & \text{or} \\ (z_2 - h_i)(z_3 - h_i) < 0 & \text{or} \\ (z_3 - h_i)(z_1 - h_i) < 0 \end{cases} \quad (\text{S11})$$

The intersection points along the edges are obtained by linear interpolation as Equ.S12, and similarly for other edges. All intersection points of the current layer form the contour point set $\mathcal{P}_i = \{P_{i1}, P_{i2}, \dots, P_{in}\}$. To obtain a smooth, ordered outer contour, the algorithm applies a **convex hull** operation. Let $\mathcal{P}_i \subset \mathbb{R}^2$ denote the 2D projection of the contour points onto the XY plane. The

convex hull is defined as the minimal convex polygon enclosing all points as Equ.S13. Once C_i is obtained, the perimeter of the contour L_i is calculated as Equ.S14, and the contour is resampled uniformly into $N = 400$ points with spacing d as Equ.S15. This procedure is repeated for all slicing planes as in Fig .S8, $d_1 = d_2 = d_3 = \dots = d_{40}$ (in Figure sampling numbers is 40, use A and D because the cross-sections B, C, and E are all circular), generating a series of evenly spaced, ordered contour layers, which serve as the basis for geometric analysis, surface reconstruction, or toolpath generation in manufacturing processes.

$$\begin{cases} P_{12} = P_1 + \frac{h_i - z_1}{z_2 - z_1} (P_2 - P_1) \\ P_{13} = P_1 + \frac{h_i - z_1}{z_3 - z_1} (P_3 - P_1) \end{cases} \quad (\text{S12})$$

$$C_i = \text{ConvexHull}(\mathcal{P}_i) = \left\{ \sum_{k=1}^m \lambda_k P_k \mid \lambda_k \geq 0, \sum_{k=1}^m \lambda_k = 1 \right\}_{\text{boundary}} \quad (\text{S13})$$

$$L_i = \sum_{k=1}^{n-1} \|P_i(k+1) - P_{ik}\| + \|P_{i1} - P_{in}\| \quad (\text{S14})$$

$$d = \frac{L_i}{N} \quad (\text{S15})$$

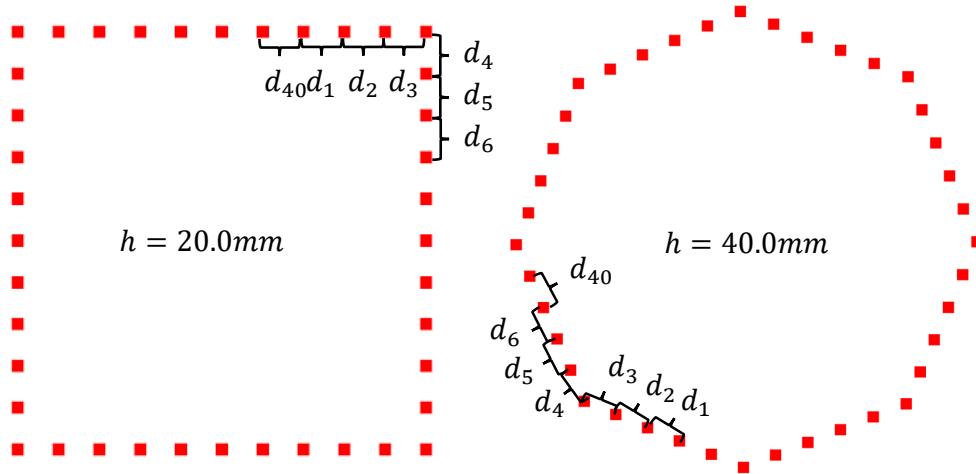


Figure S8: Single layer point cloud sampling

4.0.4 Determination of Whether a Geometry is an Enveloping Type

According to whether the geometry is of the enveloping type, different kneading methods are applied to geometries such as the cylinder, quadrangular prism, helical truncated octagonal frustum, Slim waist, and concave cylinder. The geometric body is considered an enveloping shape when it simultaneously satisfies the following three criteria: continuity of average radius gradient as Equ.S16, monotonicity of cross-sectional area as Equ.S17, and regularity of torsion angle as Equ.S18. While geometry satisfy $\frac{d\bar{r}}{dz}$, $\frac{dA}{dz}$ and $f(z)$ is continuous, the geometry is considered an enveloping geometry.

$$\bar{r}(z) = \frac{1}{2\pi} \int_0^{2\pi} r(z, \theta) d\theta, \quad \frac{d\bar{r}}{dz} \quad (\text{S16})$$

$$A(z) = \int_0^{2\pi} r^2(z, \theta) d\theta, \quad \frac{dA}{dz} \quad (\text{S17})$$

$$\frac{d\theta}{dz} = f(z), \quad (\text{S18})$$

The circumscribed radius of the sections, section centers, rotational/symmetry properties, and enveloping status of the five geometric bodies are shown in the Tab.S1.

| Index | Variation of Circumscribed Radius | Section Center Variation | Symmetry Property | Enveloping Shape |
|-------|-----------------------------------|--------------------------------------|---|------------------|
| A | Constant | Fixed | Axial, Central Symmetry | True |
| B | Constant | Coaxial | Axial, Central, and Rotational Symmetry | True |
| C | Continuous variation | Coaxial | Rotational Symmetry | False |
| D | Linear Variation | Fixed Axis | Rotational Symmetry along Axis | True |
| E | Constant | Center Translates on Plane along z | Axial Symmetry | False |

Table S1: Geometry Classification

4.0.5 Envelope shaping first

The PCL data are organized into layers according to height, and each layer contains $N_h = 400$ points as Equ.S19. Convert the point $(x_{h,i}, y_{h,i})$ into polar coordinates as Equ.S20, where $r_{hi} = D_{hi}$. A symmetric pairing is established between the left and right fingers as Equ.S21, $\{D_{hi}\}_{i=1}^{N'_h} = L_h \cup R_h$. During the kneading process, the turntable rotates over a full circle, while Equ.S21 only represents half of the rotation. For the other half, the PCL data of the left and right fingers are swapped.

$$P = \bigcup_{h=1}^{H_{\max}} P_h, \quad \text{where } P_h = \{(x_{h,i}, y_{h,i}, z_{h,i}) \mid z_{h,i} = h, i = 1, \dots, N_h\}. \quad (\text{S19})$$

$$\begin{cases} r_{hi} = \sqrt{x_{hi}^2 + y_{hi}^2} = D_{hi} \\ \theta_{hi} = \text{atan2}(y_{hi}, x_{hi}) \in (-\pi, \pi] \\ z_{hi} = h \end{cases} \quad (\text{S20})$$

$$\begin{cases} L_h = \{D_{h1}, \dots, D_{h, \frac{N'_h}{2}}\} \\ R_h = \{D_{h, \frac{N'_h}{2}+1}, \dots, D_{h, N'_h}\} \end{cases} \quad (\text{S21})$$

The kneading–forming process is characterized by a layer-by-layer gradual transition. To prevent over-compression or under-forming during shaping, a molding compensation term is introduced into the end-effector displacement as a global correction parameter, as Equ.S22, the W is left and right finger in ideal state width. The ideal volume of the molded object is calculated as Equ.S23, h_k is the max radius of k layers, The compensated volume is given by Equ.S24, $D'(h_k)$ represents the maximum radius of the current k -th layer following the compensation.

$$D_{hi}^{\text{raw}} = \frac{W}{2} - |D_{hi} - s| - m \quad \text{where } m = \text{mold_scale}. \quad (\text{S22})$$

$$V_{\text{orig}} = \sum_{k=1}^n \pi D(h_k)^2 \cdot \Delta h, \quad (\text{S23})$$

$$\begin{cases} D'(h_k) = D(h_k) + \Delta r \\ V_{\text{scaled}} = \sum_{k=1}^n \pi D'(h_k)^2 \cdot \Delta h \end{cases} \quad (\text{S24})$$

To improve the kneading efficiency, the radius is increased while keeping the volume constant, and the height is recalculated according to the volume ratio. First calculated origin volume and scaled volume ratio as Equ.S25, H' denotes the height to be kneaded as Equ.S26. By calculating the circumference of the PCL C_h as Equ.S27 in the current layer after compensation and dividing it by the diameter of the end-effector d_m , the number of kneading operations required for the current layer is obtained as Equ.S28. The kneading step size is then determined based on this number of operations as Equ.S28, while m zero is the final forming stage of kneading, the value of K_h is calculated base on $d_m/2$. In the last kneading command is $(h, i, D_{hi}^{\text{raw}}, i + N'_h/2, D_{h, i+N'_h/2}^{\text{raw}})$.

$$\alpha = \frac{V_{\text{orig}}}{V_{\text{scaled}}} \quad (\text{S25})$$

$$H' = \{h'_1, h'_2, \dots, h'_n \mid h'_k = h_1 + \alpha (h_k - h_1)\}. \quad (\text{S26})$$

$$C_h = 2\pi D'(h_k) \quad (\text{S27})$$

$$\begin{cases} K_h = \left\lceil \frac{C_h}{d_m} \right\rceil \\ K_h = \left\lceil \frac{C_h}{d_m/2} \right\rceil \quad \text{while } m = 0 \end{cases} \quad (\text{S28})$$

$$s_h = \max\left(1, \left\lceil \frac{N'_h}{K_h} \right\rceil\right) \quad (\text{S29})$$

4.0.6 Similar gradient method

The similar gradient method is a manufacturing approach based on maintaining local consistency of shape across adjacent layers. Its core principle is to achieve global continuity and controllability of deformation through gradual variation between neighboring points or cross-sections. Calculate the cross-sectional area of each layer of the PCL based on its polar coordinate data as Equ.S30, then

sum the every layers area as Equ.S31, compressed ration calculate as S25. Compressed $H_{\max}^{\text{compressed}}$ calculate as Equ.S32, map the points of the compressed layer $H_k^{\text{compressed}}$ to the nearest original layer H^{scaled} .

$$\begin{cases} A_h &= \frac{1}{2} \sum_{i=1}^{n_h} r_i r_{i+1} \sin(\theta_{i+1} - \theta_i), \quad r_1 = r_{n_h+1}, \theta_1 = \theta_{n_h+1} \\ A_h^{\text{scaled}} &= \frac{1}{2} \sum_{i=1}^{n_h} r_i^{\text{new}} r_{i+1}^{\text{new}} \sin(\theta_{i+1} - \theta_i) \end{cases} \quad (\text{S30})$$

$$\begin{cases} V_{\text{orig}} = \sum_h A_h \\ V_{\text{scaled}} = \sum_h A_h^{\text{scaled}} \end{cases} \quad (\text{S31})$$

$$H_{\max}^{\text{compressed}} = H_{\min} + (H_{\max} - H_{\min}) \cdot \alpha \quad (\text{S32})$$

$$H_k^{\text{compressed}} = H_{\min} + k \cdot \Delta H, \quad k = 0, 1, \dots, N-1, \quad H_{N-1}^{\text{compressed}} \leq H_{\max}^{\text{compressed}} \quad (\text{S33})$$

$$\begin{cases} \text{idx} = \lfloor \frac{k}{N} \cdot N_{\text{layers}} \rfloor, \quad \text{layer_H}[\text{idx}] = H^{\text{scaled}} \\ \{(H_k^{\text{compressed}}, A_i, D_i^{\text{raw}})\}_{i=1}^{n_{\text{layer}}} \end{cases} \quad (\text{S34})$$

4.0.7 From Point Cloud to Kneading Command: Overview

The proposed kneading instruction generation algorithm first extracts PCL data from the STL mesh model through layer-based slicing and converts it into a polar coordinate representation for geometric analysis. Based on the continuity of the average radius gradient, the monotonicity of the cross-sectional area, and the regularity of the torsion angle, the geometry is classified as either enveloping or non-enveloping. For enveloping geometries, the Envelope Shaping First method is applied, whereas the Similar Gradient Method is used for non-enveloping geometries.

Subsequently, the kneading path is adaptively generated according to the minimum-radius principle and the geometric characteristics of each layer. The algorithm determines the feed and step parameters based on the end-effector diameter and radial compensation, ensuring a continuous and

volume-consistent forming process. The final output consists of an optimized kneading instruction sequence for precise and efficient shaping. Algorithm is summarized in Code 1

4.0.8 Experimental and Data Comparative Analysis

Area of the surface General ring-mesh method: core concept (continuous to discrete). In the ideal case, the surface area of a smooth surface S is given by Equ.S35, where \mathbf{n} is the normal vector of the surface. However, for a PCL, the surface is discrete and lacks a parametric equation, normal vectors, or an analytical expression.

Therefore, we approximate the surface integral using a triangular mesh of the surface is Equ.S36 where A_i is the area of the i -th triangle in the mesh and M is the total number of triangles. According to the PCL sampling method, where there are 400 points per loop with a vertical spacing of $\Delta z = 1$ mm, the PCL naturally forms a two-dimensional mesh. Here, \mathbf{v} denotes the vertices used to construct the triangles Equ.S37: let k denote the layer index along the height direction, and j denote the angular order of points on each loop, with $M = 400$ points per loop. The points between every two consecutive layers are connected to form quadrilaterals, which are then divided into two triangles as Equ.S38. here, mod denotes the modulo operation. Let the vertices of a quadrilateral be denoted as Equ.S39. The quadrilateral can then be divided into two triangles, as Equ.S40, triangles area calculates as Equ.S41. In the last, the total surface area is calculated as Equ.S42

$$A = \iint_S \|\mathbf{n}\| dS \quad (\text{S35})$$

$$A \approx \sum_{\Delta} \text{Area}(\Delta) \quad (\text{S36})$$

$$\mathbf{v}_{k,j} = (x, y, z), \quad k = 0, \dots, K, \quad j = 0, \dots, M - 1 \quad (\text{S37})$$

$$j^+ = (j + 1) \bmod M \quad (\text{S38})$$

$$Q_{k,j} = [\mathbf{v}_{k,j}, \mathbf{v}_{k+1,j}, \mathbf{v}_{k+1,j^+}, \mathbf{v}_{k,j^+}] \quad (\text{S39})$$

Algorithm 1: Adaptive Kneading Data Generation Based on Geometric Features

Input: STL mesh file, end-effector diameter d_m , blank PCL

Output: Kneading command set $Kneading_Commands$

- 1 Read STL file and extract mesh vertices;
- 2 Generate PCL $P = \{p_i(x_i, y_i, z_i)\}$ and sort by height z ;
- 3 **for** each slicing layer h_i **do**
- 4 Set layer thickness $\Delta h = 0.1$ mm;
- 5 Extract current layer PCL C_i ;
- 6 Convert C_i to polar coordinates (r_i, θ_i) ;
- 7 Compute mean radius \bar{r}_i , section area A_i , and torsion function $f(z_i)$;
- 8 Determine geometry type;
- 9 **if** $\frac{d\bar{r}}{dz}$, $\frac{dA}{dz}$, and $f(z)$ are continuous **then**
- 10 Geometry is **enveloping type**;
- 11 **else**
- 12 Geometry is **non-enveloping type**;
- 13 Select kneading method;
- 14 **if** enveloping geometry **then**
- 15 Apply *Envelope Shaping First* method;
- 16 **else**
- 17 Apply *Similar Gradient Method*;
- 18 **for** each layer **do**
- 19 Compute perimeter:
$$L_i = \sum_{k=1}^{n-1} \|P_{i,k+1} - P_{i,k}\| + \|P_{i,1} - P_{i,n}\|$$
- Resample each layer to $N = 400$ points;
- 20 Generate kneading commands based on minimum radius principle:

$$\Delta r_{\max} = R_{blank}^{\max} - R_{mold}^{\min}$$

- 21 **if** $\Delta r_{\max} \neq 0$ **then**
 - 22 $height_step = d_m - 1$, $radial_step = d_m$;
 - 23 **while** $\Delta r_{\max} > 0$ **do**
 - 24 Perform kneading with feed depth = 1 mm;
 - 25 $\Delta r_{\max} \leftarrow \Delta r_{\max} - 1$;
 - 26 **else**
 - 27 $height_step = d_m/2$, $radial_step = d_m/2$;
 - 28 Output final kneading commands $Kneading_Commands$;
-

$$\Delta = \begin{cases} \Delta_1 = (\mathbf{v}_{k,j}, \mathbf{v}_{k+1,j}, \mathbf{v}_{k+1,j^+}) \\ \Delta_2 = (\mathbf{v}_{k,j}, \mathbf{v}_{k+1,j^+}, \mathbf{v}_{k,j^+}) \end{cases} \quad (\text{S40})$$

$$\text{Area}(T) = \frac{1}{2} \|(B - A) \times (C - A)\| \quad (\text{S41})$$

$$A_{\text{surface}} \approx \sum_{k=0}^{K-1} \sum_{j=0}^{M-1} \left[\frac{1}{2} \|(\mathbf{v}_{k+1,j} - \mathbf{v}_{k,j}) \times (\mathbf{v}_{k+1,j^+} - \mathbf{v}_{k,j})\| + \frac{1}{2} \|(\mathbf{v}_{k,j^+} - \mathbf{v}_{k,j}) \times (\mathbf{v}_{k+1,j^+} - \mathbf{v}_{k,j})\| \right] \quad (\text{S42})$$

4.0.9 Comparison of Kneaded Point Cloud

Designed three types of end-effectors as shown in Fig .S9. End-effector I ($w_m = 3 \text{ mm}$) pushes the non-kneading surface of the billet when kneading geometries C and E. End-effector II can knead geometries C and E, but after 100,000 kneading cycles, design factors cause burrs to appear on the tool head, which scratch the billet during retraction in Fig .S10. End-effector III overcomes the shortcomings of I and II, avoiding contact with the non-kneading surface and preventing material from being drawn out during tool retraction thanks to its frustum-shaped head design.

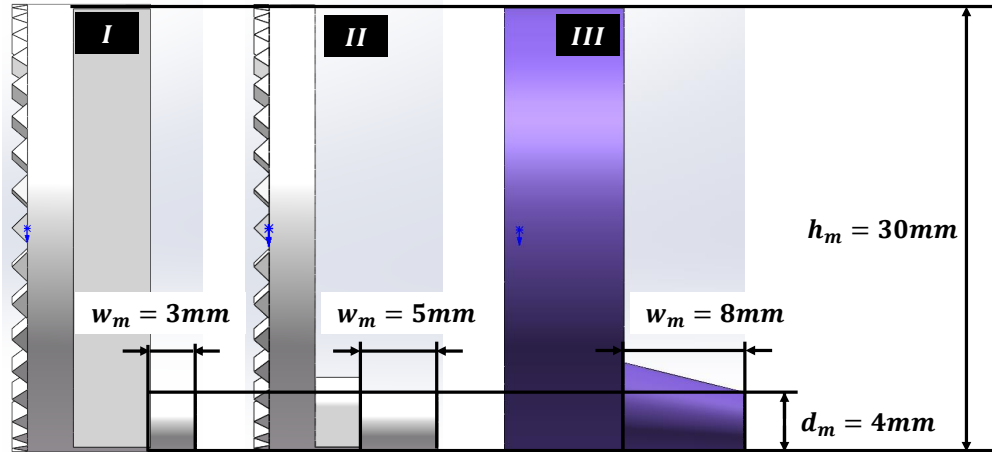


Figure S9: Three versions of End-effector

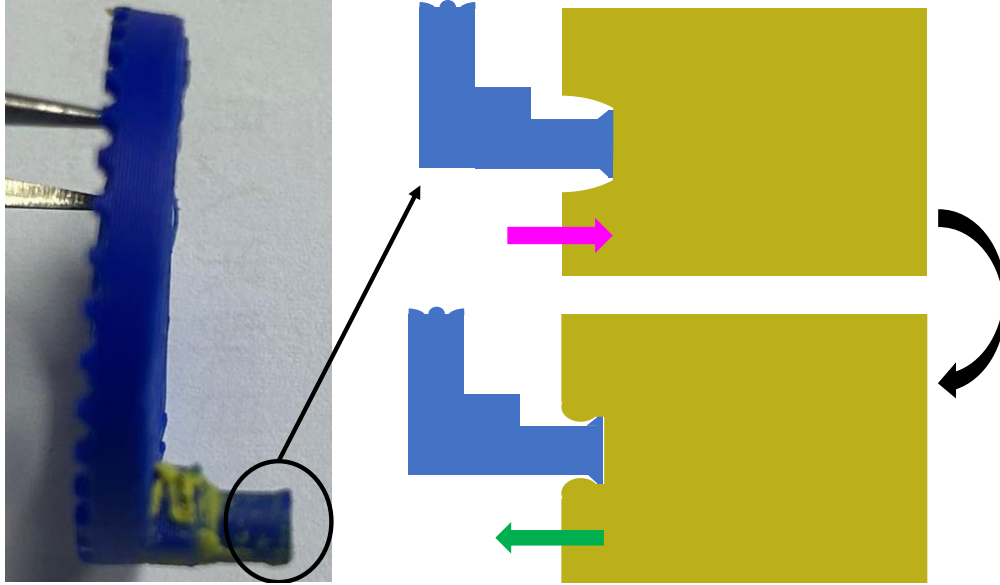


Figure S10: Retraction pulled out material

4.0.10 Ideal machining accuracy

The end-effector diameter is $d_m = 4mm$. The circular surfaces of two end-effectors are perpendicular to XOY plane and parallel to XOZ plane, moving horizontally toward each other along the Y-axis, as Fig .S11.

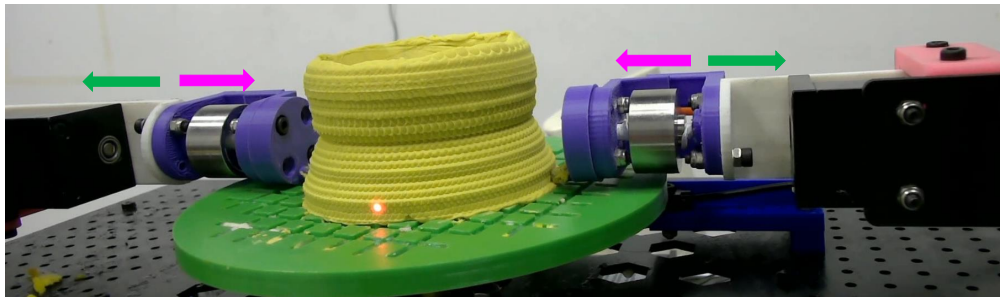


Figure S11: End-effector reciprocating motion

kneading is performed layer by layer, and the actual kneading range for each layer is shown in Fig .S12. I shows the kneading range of the end-effector at $layer_i$. After the kneading of $layer_i$ is completed, $layer_{i+1}$ is molded as shown in II. III illustrates the effective PCL ranges of $layer_i$ and $layer_{i+1}$. When the molding of $layer_{i+1}$ is completed, only the lower half of the end-effector's molding range in $layer_i$ remains effective (since the molding is performed layer by layer from bottom to top, only the lower half is active).

Therefore, according to the situation shown in Fig .S8 and based on the molding commands generated in Sec 4.0.5 and Sec 4.0.6, the kneading command is used to construct the ideal machining PCL mapped onto the end-effector.

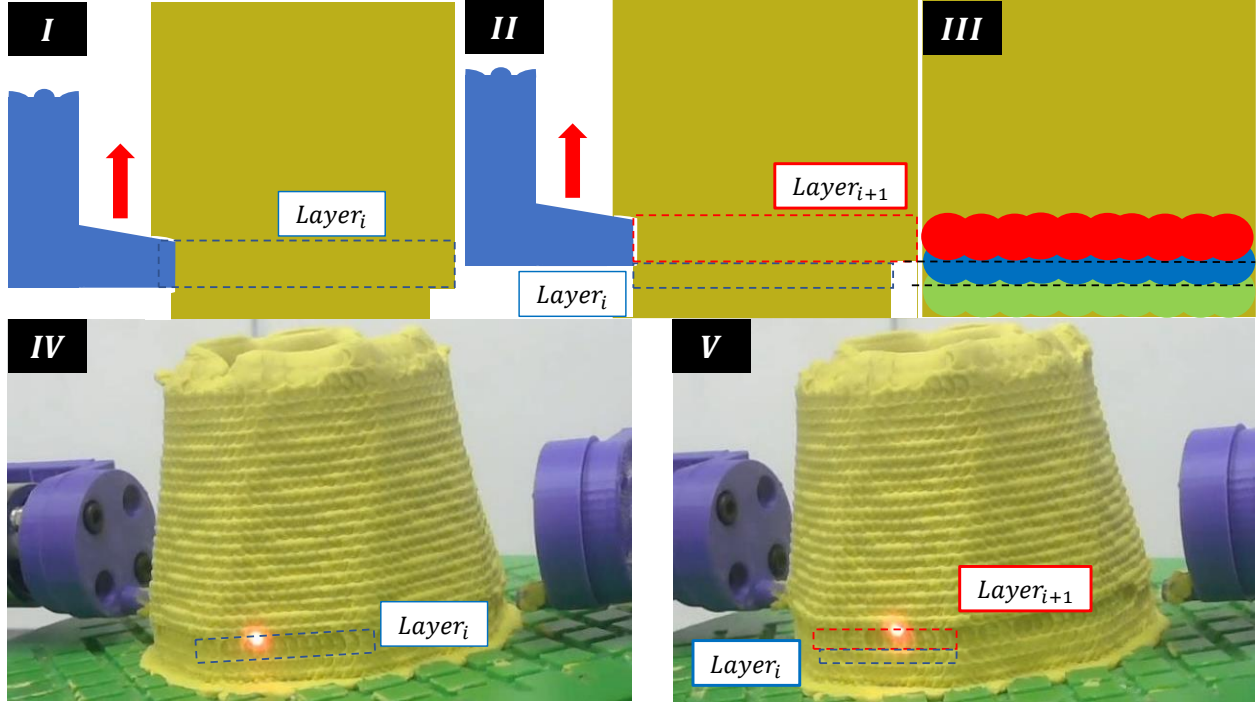


Figure S12: Actual Knead range

The commands $(h, i, D_{hi}^{\text{raw}}, i+N'_h/2, D_{h,i+N'_h/2}^{\text{raw}})$ are inversely used to generate a PCL. Then, for each point in the cloud, a semicircular PCL representing the actual effective area of the end-effector is generated, with each semicircle centered at the corresponding point, perpendicular to XOY plane. Get one point from PCL, is the circle center c_i , the normal vector \mathbf{n}_i of the circular surface is the unit vector from the circle center pointing toward the Z-axis, let \mathbf{u}_i and \mathbf{v}_i be two unit vectors lying in the plane, perpendicular to each other and perpendicular to the normal vector, because the circle plane perpendicular to XOY plane, so can use the \mathbf{u}_i is $(\mathbf{0}, \mathbf{0}, \mathbf{1})$, as Equ.S43. Then assume generates N_{gp} points within the circular area of diameter d_m end-effector, each generated circular ring is r_{gpi} , as Equ.S44. The number of points on each circular ring varies with the radius (to ensure approximately uniform point density along the ring) as Equ.S45, K represents the minimum number of points on each circular ring, to avoid shape distortion caused by overly sparse sampling near the center of the ring, K is typically set to 8, 12, or 16. Points on each ring are evenly distributed in angle as Equ.S46. In the end the uniformly distributed PCL coordinates $\mathbf{p}_{k,j}$ generated with c_i as the circle

| Geometric | Threshold | RMSE |
|-----------|-----------|-------|
| A | 2.3 | 0.895 |
| B | 1 | 0.316 |
| C | 1.1 | 0.404 |
| D | 1.1 | 0.407 |
| E | 1.2 | 0.448 |

Table S2: Ideal machining PCL and Target PCL ICP registration results

center are show in Equ.S47.

$$\mathbf{v}_i = \frac{\mathbf{n}_i \times \mathbf{u}_i}{\|\mathbf{n}_i \times \mathbf{u}_i\|} \quad (\text{S43})$$

$$r_{\text{gpi}} = \frac{d_m * k}{2 * \text{int}(\sqrt{N_{gp}})}, \quad k = 1, 2, \dots, \sqrt{N_{gp}} \quad (\text{S44})$$

$$n_{\text{points},k} = \max \left(K, \text{int} \left(\frac{2\pi r_k}{R/(\sqrt{N_{gp}})} \right) \right) \quad (\text{S45})$$

$$\theta_j = \frac{2\pi j}{n_{\text{points},k}}, \quad j = 0, 1, \dots, n_{\text{points},k} - 1 \quad (\text{S46})$$

$$\mathbf{p}_{k,j} = \mathbf{c}_i + r_k \cos(\theta_j)\mathbf{u}_i + r_k \sin(\theta_j)\mathbf{v}_i \quad (\text{S47})$$

According to Equ.S47, the generated ideal machining PCL(set $N_{gp} = 40$) is shown in Fig .S13. A, B, and D are placed in the first layer because they are processed using the enveloping method, C and E are placed in the second layer because they are processed using the similarity method.

The ideal machining PCL and the target PCL extracted from the STL model were registered using the ICP algorithm. By adjusting the distance threshold, the fitness was optimized to 1.0. The ideal machining accuracy was evaluated using the obtained root mean square error (RMSE). The variations of ICP registration results with distance threshold for the five geometries A, B, C, D, and E are shown in . Final registration results of the five geometric objects are shown in the Tab .S2.

Geometric A and B kneaded PCL and compensation PCL ICP registration result The registration result of the actual kneaded PCL for geometric object A is shown in Fig .S14- K_A .

| Geometric | Kneading Method | Threshold | RMSE |
|-----------|-----------------|-----------|-------|
| A | K_A | 14.8 | 2.802 |
| | I_A | 2.3 | 0.895 |
| | $K_{Scale-A}$ | 16.9 | 1.202 |
| | AM_A | 1.0 | 0.392 |
| B | K_B | 14.3 | 2.487 |
| | I_B | 1 | 0.316 |
| | $K_{Scale-B}$ | 16.9 | 1.16 |
| | AM_B | 1.2 | 0.657 |
| C | K_{C1} | 3.4 | 1.977 |
| | K_{C2} | 3.6 | 1.799 |
| | I_C | 1.1 | 0.404 |
| | $K_{Scale-C1}$ | 1.7 | 0.545 |
| | $K_{Scale-C2}$ | 2.8 | 0.722 |
| | AM_C | 2.3 | 0.832 |
| D | K_{D1} | 3.8 | 1.86 |
| | K_{D2} | 4.2 | 1.567 |
| | I_D | 1.1 | 0.407 |
| | $K_{Scale-D1}$ | 2.5 | 0.56 |
| | $K_{Scale-D2}$ | 5.6 | 0.71 |
| | AM_D | 1.8 | 0.622 |
| E | K_{E1} | 12.8 | 2.445 |
| | K_{E2} | 12.8 | 2.462 |
| | I_E | 1.2 | 0.448 |
| | $K_{Scale-E1}$ | 15.8 | 0.76 |
| | $K_{Scale-E2}$ | 15.7 | 1.268 |
| | AM_E | 1.9 | 0.768 |

Table S3: Geometry ICP Registration between Actual Kneading and Compensated PCL Data

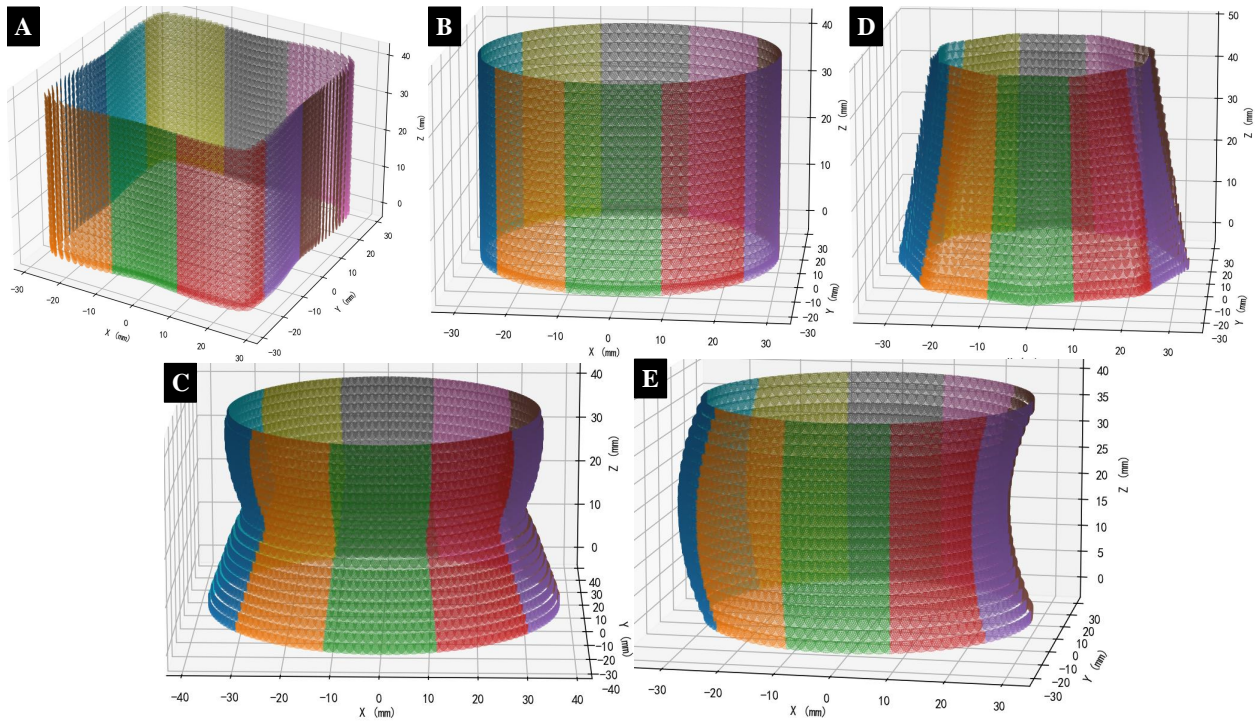


Figure S13: Ideal machining PCL

After compensating K_A PCL with the RMSE value obtained when K_A was registered to the target PCL at Fitness 1.0 the resulting registration is shown in Fig .S14- $K_{Scale-A}$. The main source of the registration error between the kneaded PCL and the target PCL for geometric object A is highlighted in the black box in Fig. S16. This may be related to the fact that the billet has a circle prism shape. The registration result of the actual kneaded PCL for geometric object B is shown in Fig .S15- K_B . After compensating K_B PCL with the RMSE value obtained when K_B was registered to the target PCL at Fitness 1.0 the resulting registration is shown in Fig .S15- $K_{Scale-B}$. The main source of the registration error between the kneaded PCL and the target PCL for geometric object B is highlighted in the black box in Fig. S17. This may be related to the fact that the billet has a cubic prism shape.

Geometry C registered PCL and using two kneading methods model The registration results of the processed point clouds obtained using the two kneading methods for Geometry C, as well as the registration results after compensation, are shown in Fig. S18. The 3D-printed specimen and the physical parts processed using the two kneading methods are shown in Fig. S19. From the physical samples, it can be observed that K_{C1} more closely matches the 3D-printed geometry, while K_{C2}

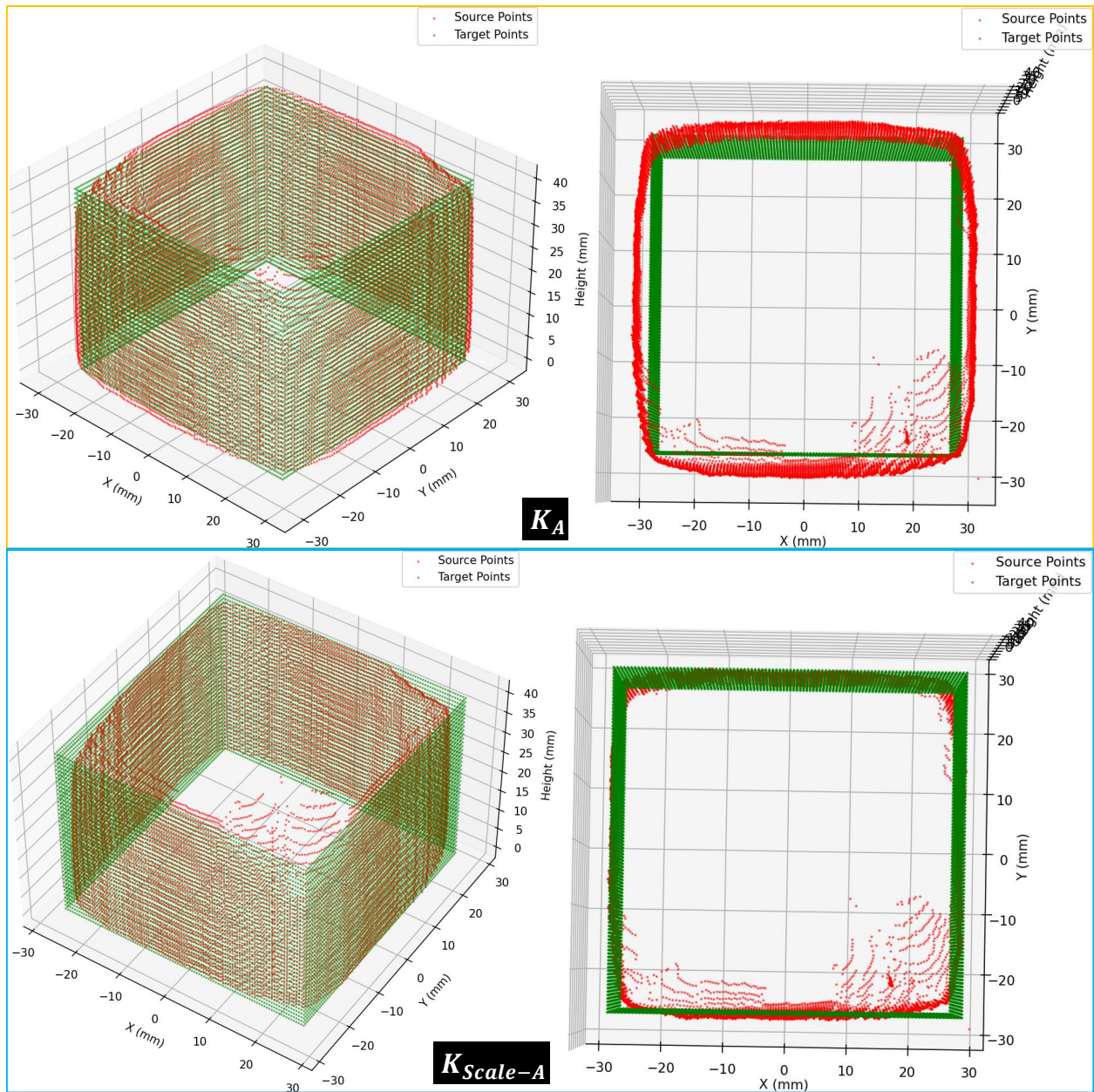


Figure S14: Geometric A: Registration results between Actual knead, Compensate PCL and Target PCL

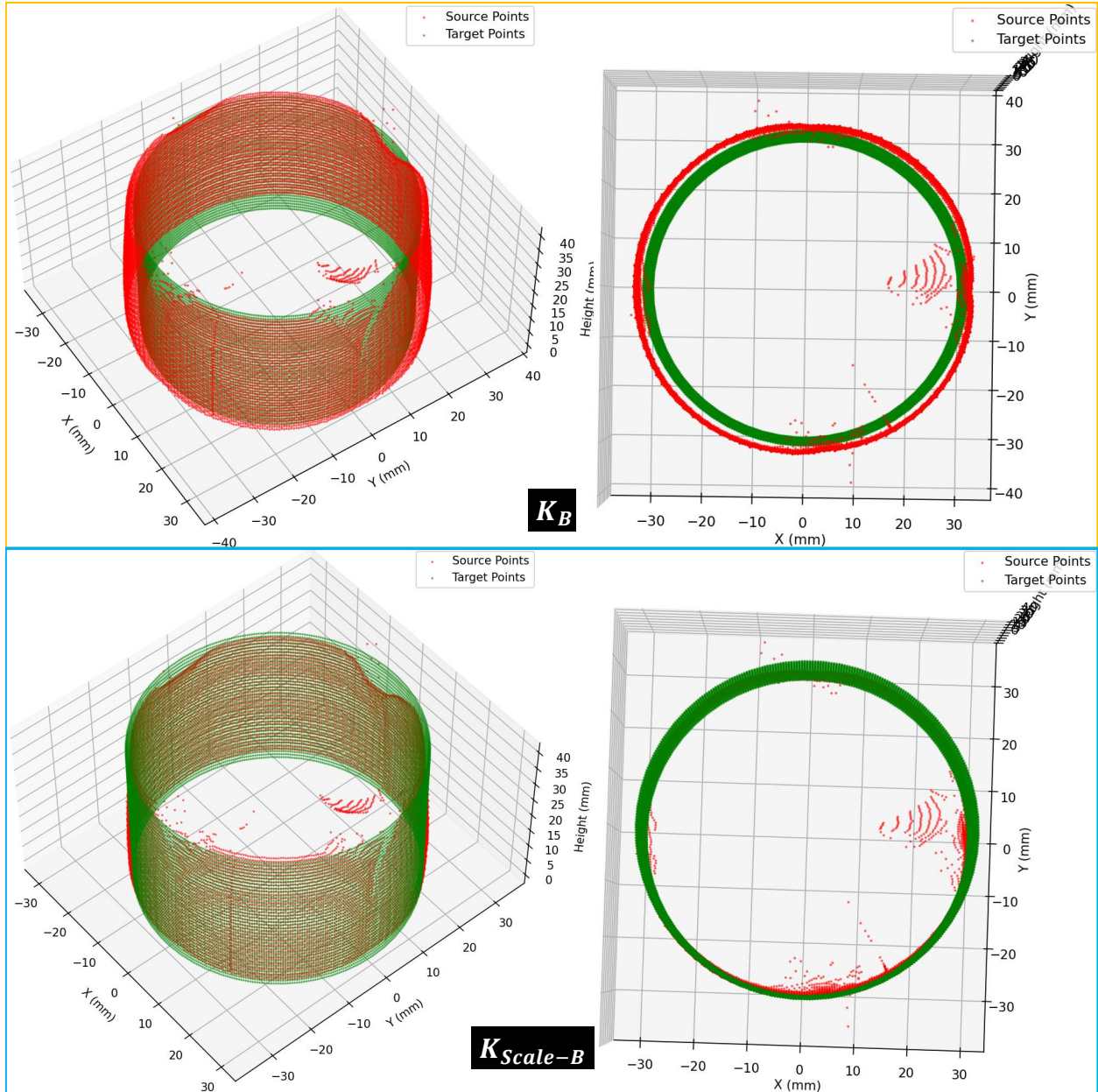


Figure S15: Geometric B: Registration results between Actual knead, Compensate PCL and Target PCL

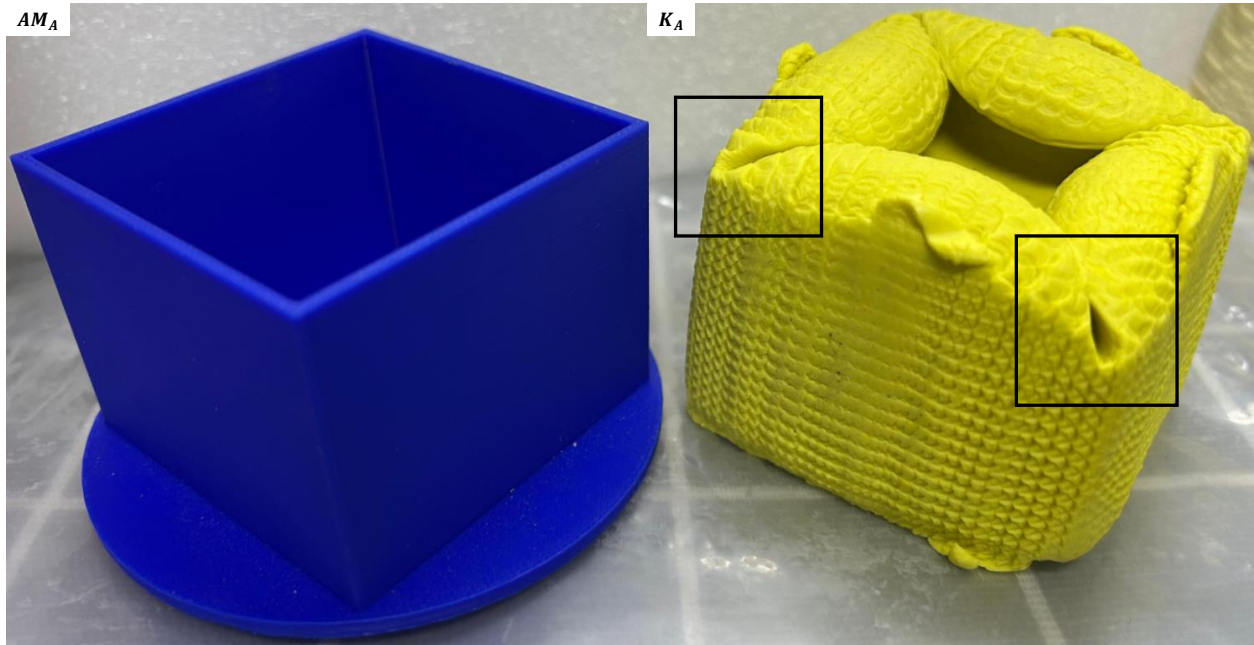
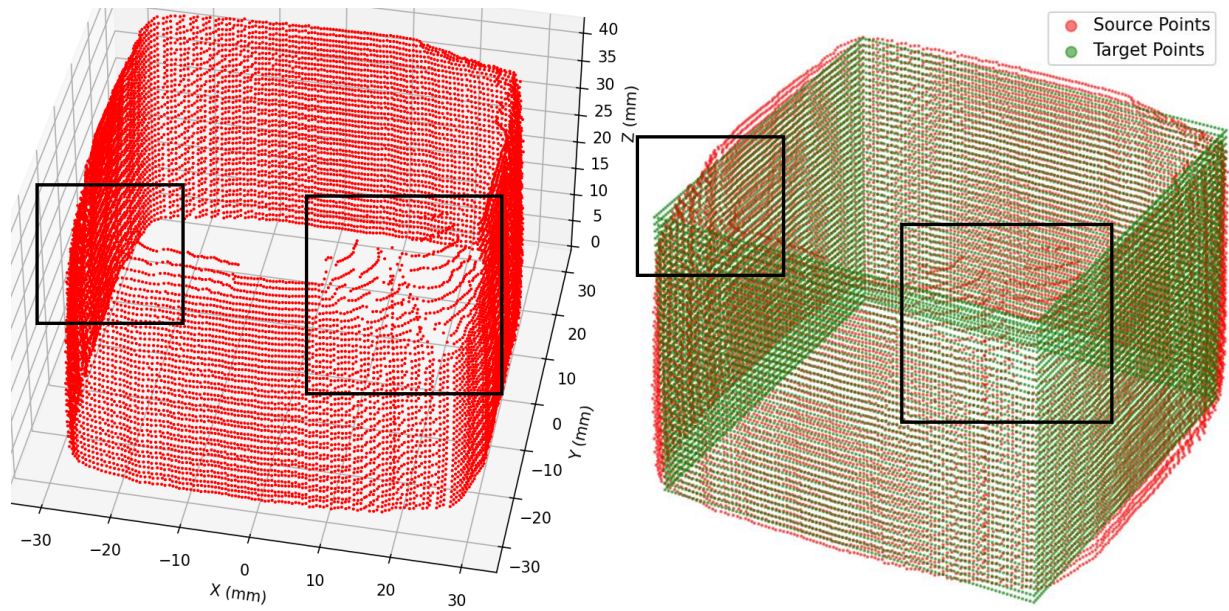


Figure S16: Geometric A kneading defect diagram

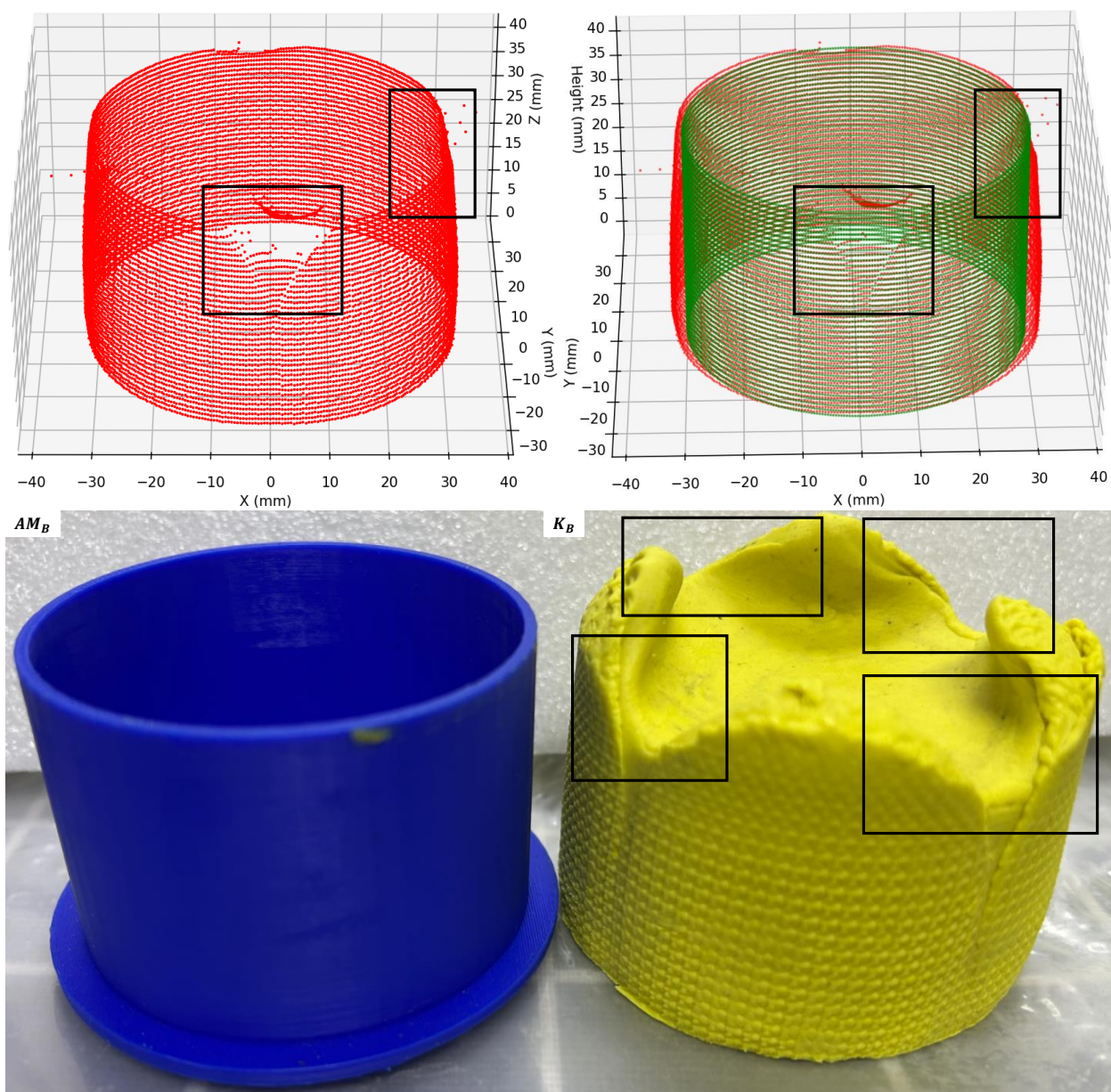


Figure S17: Geometric B kneading defect diagram

shows a noticeable discrepancy at the waist region compared with both AM_C and K_{C1} .

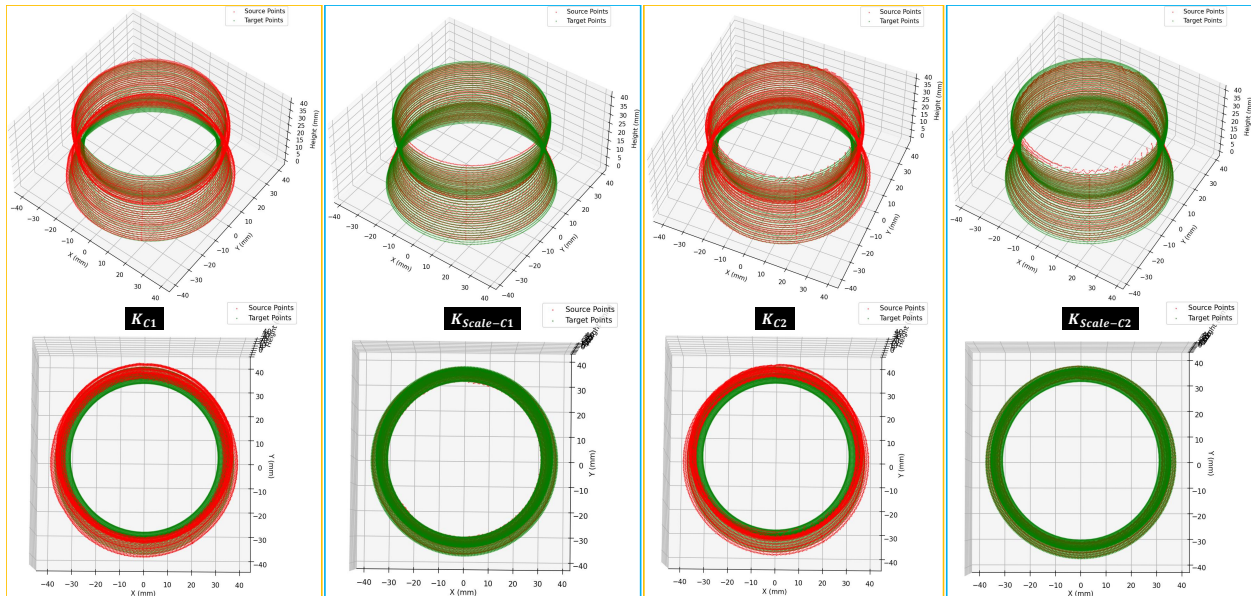


Figure S18: Geometric C: Registration results between Actual knead, Compensate PCL and Target PCL



Figure S19: Geometric C: 3D-printed and Two kneading methods

Geometry D registered PCL and using two kneading methods model The registration results of the machined point clouds obtained from the two kneading methods for Geometry D, as well as the registration results after compensation, are shown in Fig. S20. The 3D-printed model and the physical objects machined using the two kneading methods are presented in Fig. S21. From the physical objects, it can be observed that both K_{D1} and K_{D2} are close to AM_D , with K_{D1} appearing visually closer.

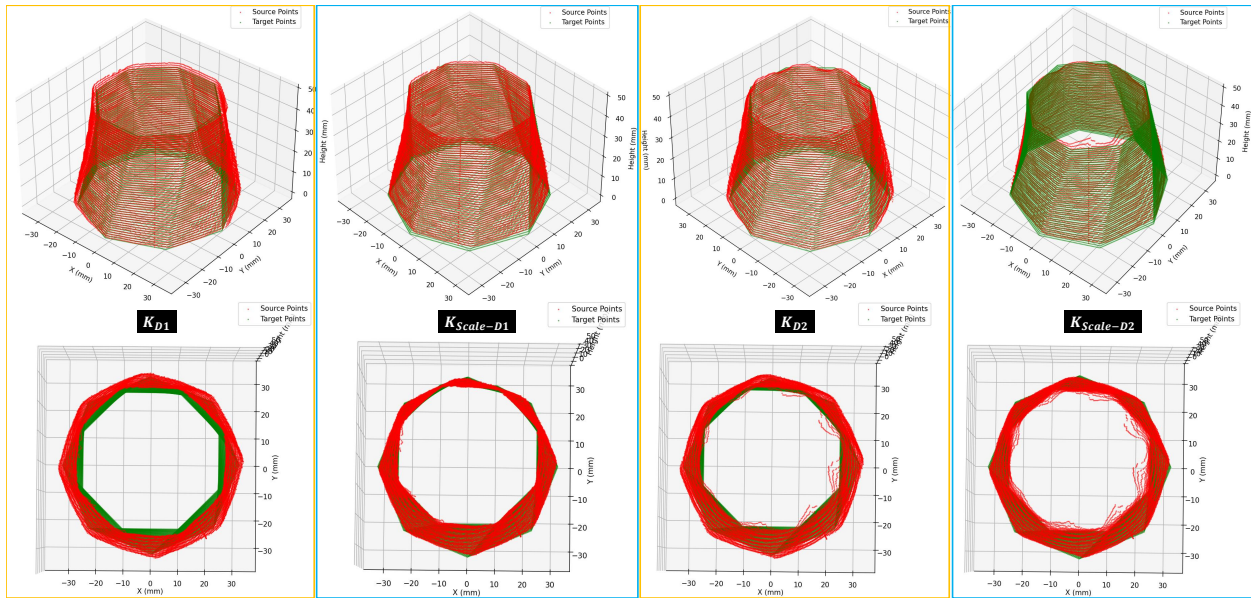


Figure S20: Geometric D: Registration results between Actual knead, Compensate PCL and Target PCL



Figure S21: Geometric D: 3D-printed and two kneading methods

Geometry E registered PCL and using two kneading methods model The registration results of the machined point clouds obtained from the two kneading methods for Geometry E, as well as the registration results after compensation, are shown in Fig. S22. The 3D-printed model and the physical objects machined using the two kneading methods are presented in Fig. S23. From the physical objects, no obvious difference can be observed between K_{E1} and K_{E2} .

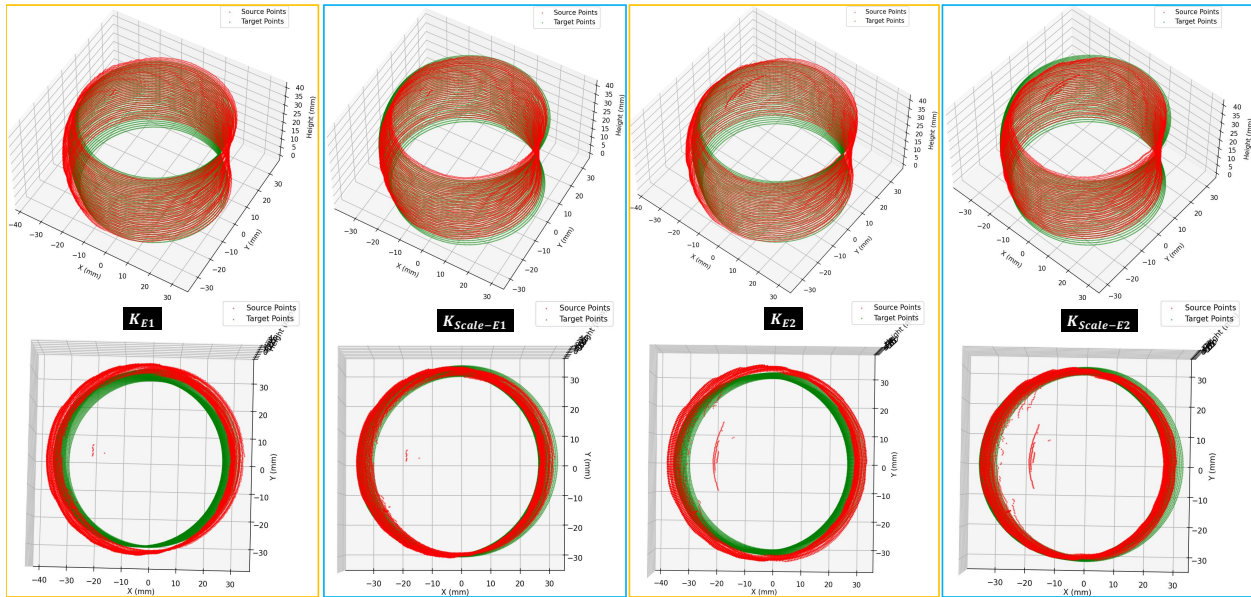


Figure S22: Geometric E: Registration results between Actual knead, Compensate PCL and Target PCL



Figure S23: Geometric E: 3D-printed and two kneading methods